## PAPER

Check for updates

# Polyoxometalate-loaded reduced graphene oxide-modified metal vanadate catalysts for photoredox reactions through an indirect Z-scheme mechanism†

Soumita Samajdar,‡[ac] Gajiram Murmu,‡[bc] Maitrayee Biswas,[a] Srikrishna Manna,[cd] Sumit Saha*[bc] and Srabanti Ghosh 🆔 *[ac]

The growing energy demand and environmental concerns have accelerated research on the emergence of photocatalysts for solar fuel generation and environmental remediation. Metal vanadates, such as silver vanadate (AV) and copper vanadate (CV), are considered promising visible-light active photocatalysts owing to their narrow bandgap and suitable band structure; however, they are limited by rapid electron–hole recombination. To overcome this limitation, amalgamation with polyoxometalate (POM)-loaded reduced graphene oxide (RGO)-based novel co-catalysts is a facile strategy to improve photocatalytic performance. Herein, metal vanadates were deposited on polyoxometalate-loaded reduced graphene oxide (RPOM) *via* a one-pot coprecipitation method. The developed RPOM–AV and RPOM–CV composites exhibited photocurrent densities of 223.7 and 85.8 $\mu$A cm$^{-2}$, which were 51 times and 6 times higher than those of pristine AV and CV, respectively, owing to the remarkable augmentation in the donor density after formation of composites. Moreover, the RPOM–AV composites exhibited photocatalytic Cr(VI) reduction of up to 94% in 60 minutes with a high rate constant of 0.044 min$^{-1}$ and 94% removal of the rose bengal dye in 120 minutes through adsorption. The RPOM–CV composites demonstrated 96% photocatalytic degradation of methylene blue dye at a rate constant of 0.011 min$^{-1}$. The excellent photocatalytic activity of RPOM–metal vanadate composites was attributed to the formation of an indirect Z-scheme heterojunction between metal vanadates and POM, in which RGO acted as a suitable electron-mediator, facilitated the charge transfer, boosted the separation of photogenerated charge carriers, and lowered the electron–hole recombination. The present work provides an innovative approach toward the development of polyoxometalate-based composites for wastewater remediation.

## 1. Introduction

The elevation in the energy crisis and environmental pollution has posed a serious threat to society in the 21st century.[1–3] To resolve these challenges, solar energy harvesting *via* photocatalysis offers a viable technology for the utilization of solar energy in an eco-friendly manner.[4–6] Photocatalysis provides a promising approach towards sustainable solar-to-chemical energy conversion *via* solar fuel generation as well as environmental remediation through the photodegradation of various pollutants in the presence of light.[7–11] Hence, there is an urgent need for the development of visible-light active photocatalysts that could be employed for various photocatalytic applications, such as H$_2$ generation *via* water splitting,[12] CO$_2$ photoreduction,[13] N$_2$ fixation,[14] and environmental remediation *via* organic dye and heavy metal removal.[15,16]

As an alternative to wide bandgap semiconductors, metal vanadates, particularly silver and copper vanadates, have gained immense attention in photocatalysis.[17–20] They exhibit a lower bandgap suitable for visible light absorption, suitable band structure, exceptional chemical stability, high crystallinity, and non-toxic nature. For example, our group fabricated

[a] *Energy Materials & Devices Division, CSIR – Central Glass and Ceramic Research Institute, Kolkata, West Bengal 700032, India. E-mail: srabanti@cgcri.res.in*

[b] *Materials Chemistry & Interfacial Engineering Department, CSIR – Institute of Minerals & Materials Technology, Bhubaneswar, Odisha 751013, India. E-mail: sumitsaha@immt.res.in*

[c] *Academy of Scientific and Innovative Research (AcSIR), Ghaziabad, Uttar Pradesh 201002, India*

[d] *Specialty Glass Division, CSIR – Central Glass and Ceramic Research Institute, Kolkata, West Bengal 700032, India*

† Electronic supplementary information (ESI) available. See DOI: https://doi.org/10.1039/d4ya00535j

‡ Equal contributions.

metallic Ag nanoparticles anchored to 1D AgVO$_3$ nanorods on 2D MoS$_2$ nanosheets. The as-synthesized nanocomposites with 1D/2D interface exhibited a high rate of photocatalytic H$_2$ generation ($\sim$38.6 mmol g$^{-1}$) as a result of the development of an all-solid-state Z-scheme heterojunction with Ag nanoparticles acting as the electron mediator.[21] In another study, Yu et al. synthesized irregular hexagon-shaped ternary AgVO$_3$/Ag$_4$V$_2$O$_7$/BiOI heterojunction via a one-step hydrothermal method.[22] It was observed that the as-synthesized composites resulted in the 100% and 45% photodegradation of methylene orange and tetracycline antibiotic, respectively, within 80 minutes owing to the development of a double S-scheme heterojunction, which promoted effective charge transfer and lowered the electron–hole recombination. The photoelectrochemical (PEC) water splitting by copper vanadates as photoanodes was investigated by Jiang et al.,[23] and it was observed that the copper vanadates with different Cu:V elemental ratios exhibited higher photocurrent densities ($\sim$0.206 mA cm$^{-2}$), with much stronger visible light absorption and better charge separation efficiencies. However, pristine metal vanadates suffer from various disadvantages, such as photo corrosion on long-term light exposure, rapid electron–hole recombination, and low quantum yield, which leads to poor photocatalytic performance.[24] To circumvent these drawbacks, several strategies can be adopted, including defect modulation, vacancy engineering, heterostructure construction, and co-catalyst loading.[25–27]

However, polyoxometalates are an emerging class of transition metal–oxygen anion nanoclusters, which have introduced new horizons in the field of photocatalysis owing to several benefits. They consist of abundant surface-exposed active sites, tuneable band gaps, an easily modifiable framework, and superior redox properties.[28–30] However, most pristine polyoxometalates have a wide bandgap, capable of only UV radiation absorption, as well as a low specific surface area, which limits their photocatalytic efficiency.[31] These limitations can be overcome by combining polyoxometalates with two-dimensional materials, such as reduced graphene oxide. Reduced graphene oxide possesses excellent electron mobility that can facilitate the continuous transfer of photogenerated charge carriers and, therefore, can act as a solid-state electron mediator.[32,33] Moreover, the large surface area of RGO makes it a good support material for anchoring the polyoxometalates.[34] The combination of RGO with POM may enhance visible light absorption, improve electron transfer, and increase the number of active sites. For example, Gao et al.[35] synthesized a set of three-component materials, AgBr/polyoxometalate/graphene oxide (AgBr/POM/GO) composites, by employing a hydrothermal technique assisted by an ionic liquid. It was observed that AgBr/PMo$_{12}$/GO exhibited a remarkably high rate of photocatalytic H$_2$ generation ($\sim$256 µmol g$^{-1}$ h$^{-1}$) attributable to the excellent redox properties of POMs. Interestingly, Li et al.[36] explored the rate of photocatalytic N$_2$ fixation using POM-based RGO composites (RGO@H$_5$[PMo$_{10}$V$_2$O$_{40}$]). It was observed that the as-synthesized composites resulted in a superior rate of NH$_3$ generation of $\sim$130.3 µmol L$^{-1}$ h$^{-1}$, which is 97.3% higher than that of pristine POM, as the introduction of RGO facilitates electron transfer and suppresses the rate of electron–hole pair recombination. In another study, Yu et al.[37] obtained 84.02% removal of methylene blue dye within 150 minutes with the help of polyoxometalate-graphene oxide composites as a result of the establishment of the Z-scheme heterojunction, which favors spatial segregation of the charge carriers.

Although polyoxometalate-based graphene composites have been explored for electrocatalysis applications, their applications in photocatalysis are marked by a significant scarcity. To the best of our knowledge, the combination of metal vanadates with polyoxometalate-loaded reduced graphene oxide-based photocatalysts has not yet been reported. The novelty aspect of our study comprises the exploration of the photoelectrochemical properties and photocatalytic activity of the polyoxometalate-loaded reduced graphene oxide–metal vanadate composites. The interfacial charge transfer between POM and metal vanadates via an indirect Z-scheme mechanism was investigated for the first time. In the present work, polyoxometalate-loaded reduced graphene oxide was successfully amalgamated with metal vanadates, such as silver vanadate (AV) and copper vanadate (CV), via a facile one-pot coprecipitation approach. Excellent charge separation and lower charge-carrier recombination are examined with the help of photoelectrochemical analysis and photoluminescence spectral studies. The superior photocatalytic activity towards Cr(VI) reduction and organic dye removal occurs owing to excellent charge transfer through the indirect Z-scheme heterojunction, with RGO acting as the electron mediator between the metal vanadates and POM.

## 2. Experimental section

### 2.1. Materials and methods

The synthesis of all the materials was carried out at room temperature. Sodium tungstate dihydrate, Na$_2$WO$_4$·2H$_2$O (99%), silver nitrate (AgNO$_3$, 99%), ammonium metavanadate (NH$_4$VO$_3$, 99%), and copper(II) acetate dihydrate (Cu(OAc)$_2$·2H$_2$O) were procured from Sigma-Aldrich. Methyltriphenyl phosphonium bromide (99%) and anhydrous N,N-dimethylformamide (ACS grade 99.8%) were purchased from Alfa-Aesar. Hydrochloric acid (ACS grade) was purchased from Finar. Acetic anhydride (Ac$_2$O) was purchased from Pallav Chemicals. Ethanol (99.8%) was purchased from Himedia. Diethyl ether (99%) was purchased from Merck. Deionized (DI) water (18.2 MΩ cm) was obtained from the Millipore system.

Powder X-ray diffractograms (PXRD) of the as-synthesized composites were recorded using a Philips X'Pert diffractometer with Cu Kα radiation at a slow scan rate of 1° min$^{-1}$. A Thermo Nicolet 6700 spectrophotometer was employed to obtain the FT-IR spectra within a range of 400–4000 cm$^{-1}$. The Raman spectra were obtained using a Micro Raman setup (Renishaw InVia Reflex Raman spectrometer) with an excitation line of 785 nm. NETZSCH, STA 449 F3, Jupiter was employed to carry

out the thermogravimetric analysis (TGA) at temperatures ranging from 30 °C to 900 °C. UV-Visible absorption spectra were recorded with the help of an evolution-one plus spectrophotometer within a wavelength range of 200–900 nm. Solid phase DRS spectra were performed using a JASCO V-670 spectrometer in the 200–900 nm range. JEOL JSM IT 800 SHL was employed to record the field emission scanning electron microscopy (FESEM) images, and EDAX and elemental mapping were obtained using the EDAX-Octane Elect. JEOL JEM F200 with an EDS (Oxford) and Rio-16 Gatan camera was used to capture the high-resolution transmission electron microscopy (HRTEM) images. The degradation of dye was carried out in the presence of Luzchem LZC-4 × 112 W cool white fluorescent tubes. The X-ray photoelectron spectroscopy (XPS) measurements were performed using a PHI 5000 Versa Probe III spectrophotometer. Quantachrome, FL-314.326, was employed to determine the $N_2$ adsorption–desorption isotherm.

## 2.2. Synthesis of $(MePh_3P)_2W_6O_{19}$ (POM)

The novel phosphonium hexatungstates were synthesized from sodium tungstate and modified by substituting phosphonium bromide salt for the analogous tetraalkylammonium salt.[38] A 1.0 g of sodium tungstate dihydrate ($Na_2WO_4 \cdot 2H_2O$), 5 mL of $Ac_2O$, and 4 mL of DMF were poured into a 50 mL Erlenmeyer flask under continuous magnetic stirring at 100 °C for three hours. This led to the formation of a creamy-white suspension, followed by the addition of 2 mL of $Ac_2O$ and 1.8 mL of 12 M hydrochloric acid in 5 mL of DMF under magnetic stirring. The reaction mixture was filtered using filter paper (Whatman) and washed with 5 mL of MeOH. The obtained clear filtrate was cooled to room temperature. A 507 mg of methyltriphenyl phosphonium bromide prepared in 5 mL of methanol was added to the clear filtrate under continuous stirring, which resulted in the formation of a white precipitate of bis(methyltriphenyl phosphonium)hexatungstate ($(MePh_3P)_2W_6O_{19}$) (POM).

## 2.3. Synthesis of POM-loaded reduced graphene oxide (RPOM)

The synthesis of GO was carried out using a modified Hummers' method.[39] The GO was converted to reduced graphene oxide (RGO) after hydrothermal treatment at 180 °C for 16 hours. 50 mg of RGO was dispersed in a beaker containing 30 mL of a 1 : 1 mixture of water and ethanol. In another beaker, 5 mg of POM was dispersed in 20 mL of a 1 : 1 mixture of water and ethanol. Then, this solution was added to the previous solution containing RGO, and the mixture was kept under magnetic stirring conditions for 24 hours. Then, the black precipitate was washed with water and ethanol several times and dried at a temperature of 50 °C to obtain POM-loaded RGO (RPOM).

## 2.4. Synthesis of silver-vanadate-loaded RPOM composites (RPOM–AV)

The RPOM–AV composites were synthesized using a co-precipitation strategy (Scheme 1). 35 mg of RPOM was dispersed in 35 mL DI water under ultrasonication for 30 minutes. 10 mg of $AgNO_3$ was added to the above solution under continuous magnetic stirring for 30 minutes. 5 mg of $NH_4VO_3$ was dispersed in another beaker containing 35 mL DI water. Then, the $NH_4VO_3$ solution was added dropwise into the $AgNO_3$ solution and stirred for 10 minutes at room temperature. A yellow precipitate appeared, and it was washed several times with DI water and isopropanol. After that, it was eventually dried at 50 °C to obtain the RPOM–AV1 composites. Similarly, RPOM–AV2 and RPOM–AV3 were synthesized by increasing the metal precursor loading concentration by 2 times and 3 times on RPOM, respectively.

## 2.5. Synthesis of copper-vanadate-loaded RPOM composites (RPOM–CV)

The RPOM–CV composites were synthesized via a co-precipitation strategy (Scheme 1). A 35 mg RPOM was dispersed
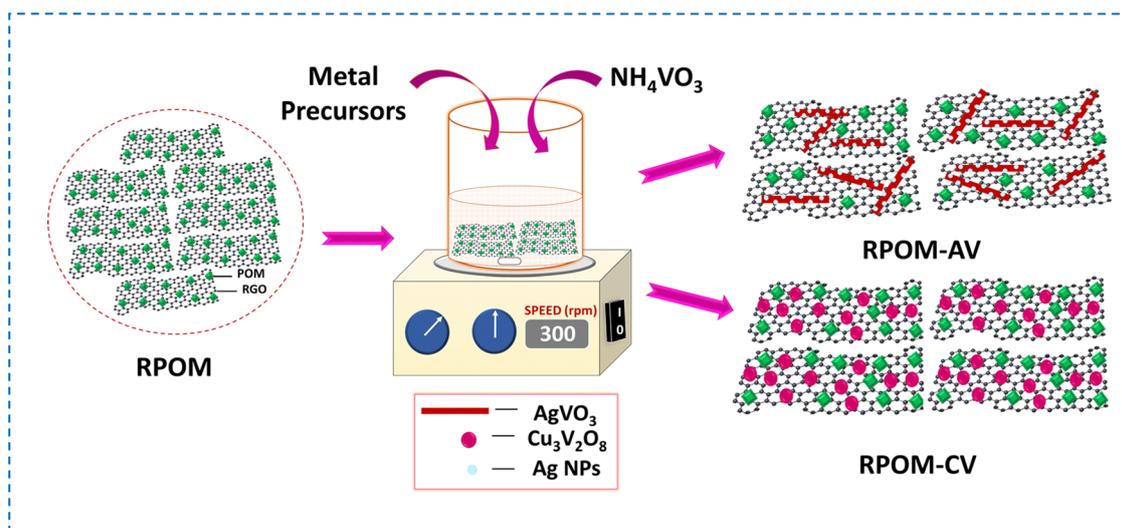


Scheme 1   Schematic of the synthesis of RPOM–AV and RPOM–CV composites via a co-precipitation method.

in 35 mL of DI water under ultrasonication for 30 minutes. 30 mg of Cu(OAc)$_2$·2H$_2$O was added into the above solution under continuous magnetic stirring for 30 minutes. 12 mg of NH$_4$VO$_3$ was dispersed in another beaker containing 35 mL DI water. Then, the NH$_4$VO$_3$ solution was added dropwise into the copper acetate solution and stirred for 10 minutes at room temperature. A dark yellow precipitate appeared, and it was washed several times with DI water and isopropanol. After that, it was eventually dried at 50 °C and subsequently calcined at 425 °C for 1 hour to obtain the RPOM–CV1 composites. Similarly, RPOM–CV2 and RPOM–CV3 were synthesized by increasing the metal precursor loading concentration by 3 times and 9 times on RPOM, respectively.

### 2.6. Photoelectrochemical measurements

To perform photoelectrochemical measurements, a spin-coater was employed to prepare thin films of the materials on FTO-coated glass slides up to 3 layers. The photoelectrochemical performance was determined with the help of a galvanostat-potentiostat (ZIVE SP1) under a 150 W Xenon lamp. A three-electrode setup was used with Ag/AgCl as the reference and Pt wire as the cathode. The current *versus* voltage spectra were recorded within the potential ranging from −0.2 V to 1.0 V *vs.* Ag/AgCl in the presence of 0.1 M Na$_2$SO$_4$ as an electrolyte. At a constant voltage of 0.6 V *vs.* Ag/AgCl, the transient photocurrent spectra were determined under light on–off conditions. Electrochemical impedance spectroscopy was used to measure the interfacial charge transfer resistance within a frequency range from 0.1 Hz to 100 kHz. To determine the junction capacitance of the electrodes, Mott–Schottky experiments were carried out by sweeping the potential from −0.8 V to 1 V *vs.* Ag/AgCl at a frequency of 1000 Hz.[40,41]

### 2.7. Photocatalytic dye degradation

The synthesized RPOM–AV3 and RPOM–CV3 hybrid composites were used to adsorb rose bengal (RB) and photocatalytic degradation of methylene blue (MB), respectively. The adsorption/degradation studies were performed with an initial dye concentration of 50 μM, catalyst loading of 0.01 mg mL$^{-1}$ (RPOM–AV3), and 1 mg mL$^{-1}$ (RPOM–CV3) under neutral pH. The RB dye adsorption was studied with a solution of RPOM–AV3 and RB dye over time. The RPOM–CV3 and MB dye solutions were irradiated with 112 W cool white fluorescent tubes under continuous stirring at varying times. The adsorption and degradation of the RB and MB dyes were measured with the help of UV-visible spectroscopy. The efficiency of degradation/adsorption of the dyes was evaluated with the help of eqn (1):

$$\text{Degradation efficiency } (\%) = \frac{C_0 - C_t}{C_0} \times 100, \quad (1)$$

where $C_0$ represents the initial concentration and $C_t$ denotes the concentration of the dye at time $t$.

### 2.8. Photocatalytic Cr(vi) reduction

The photocatalytic reduction of Cr(vi) with an initial concentration of 100 mg L$^{-1}$ was conducted in a quartz cell reactor with RPOM–AV2 composite concentration of 0.5 g L$^{-1}$ in the presence of 300 W Xenon light. Appropriate amounts of aliquots were taken up from the reactor at successive time intervals, and absorbance was recorded using a UV-visible spectrophotometer. The percentage of reduction of Cr(vi) (% RE) was evaluated with the help of the following equation:[42]

$$\% \text{ RE} = \frac{I_0 - I_t}{I_0} \quad (2)$$

where $I_0$ represents the initial intensity of absorption and $I_t$ denotes the intensity of absorption after a time interval $t$ at $\lambda_{\max} = 340$ nm.

## 3. Results and discussion

### 3.1. Powder XRD analysis

The phase purity and crystal structure of the as-synthesized composites were determined using XRD analysis. Fig. 1 portrays the powder X-ray diffractogram (PXRD) of the RPOM, bare AV, CV, RPOM–AV2, and RPOM–CV2 nanocomposites. In the case of RPOM, it is observed that the diffraction peak at 24.7° corresponds to the (002) plane of the reduced graphene oxide.[43,44] The XRD pattern of pure AV shows that the peaks at 2$\theta$ values of 22.5°, 24.9°, 27.4°, 28.2°, 31.6°, 32.1°, 32.8°, 34.9°, 39.7°, 43.6°, 46.5°, 53.2°, 55.4°, and 57.2° are well indexed to the (111), (220), (310), (22−1), (221), (−131), (002), (311), (131), (420), (240), (222), (421), and (150) planes (marked by ○) of monoclinic phase of α-AgVO$_3$, respectively (JCPDS No: 89-4396).[45] Additionally, the diffraction peaks at 38.1° and 44.2° correspond to the (111) and (200) planes of Ag$^0$ (JCPDS No: 04-0783), respectively, which indicate the presence of metallic Ag nanoparticles along with AgVO$_3$.[46] In the case of RPOM–AV2, the diffraction peaks corresponding to the monoclinic phase of α-AgVO$_3$ and metallic Ag$^0$ particles are observed. Moreover, the
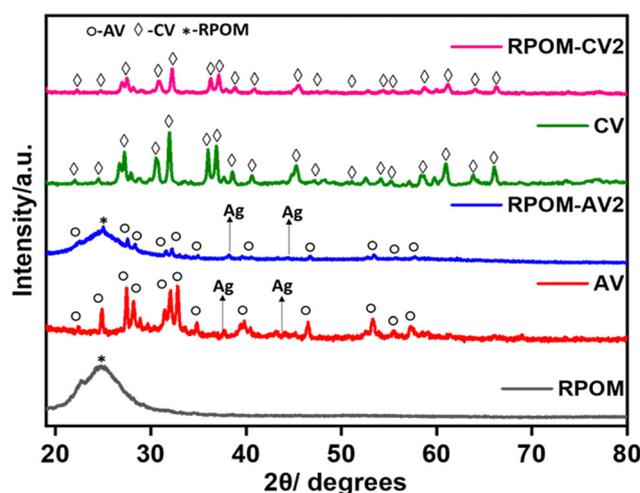


Fig. 1 PXRD pattern of RPOM, AV, RPOM–AV2, CV and RPOM–CV2.

broad peak at 24.7° in the XRD pattern of RPOM–AV2 corresponds to the (002) plane of RPOM (indicated by *). Therefore, the diffraction peaks of both RPOM and α-AgVO$_3$ in the XRD pattern of RPOM–AV2 provide evidence in favor of the nanocomposite formation. The crystallite size of AV in the RPOM–AV2 composite was calculated to be 8.0 Å by considering the most intense peak at 27.6° according to the Debye–Scherrer equation.[47] Similarly, the RPOM–AV3 composite contained the XRD patterns of bare AV and RPOM, and the peak pattern mostly matched that of the precursors, indicating the formation of the composites (Fig. S1, ESI†). The XRD pattern of the RPOM–CV2 composite portrays that the diffraction peaks corresponding to the (020), (021), (111), (200), (012), (−212), (−221), (102), (211), (040), (231), (−313), (−133), (−204), (−411), (400) and (−342) planes are present (marked by ◊), indicating that the monoclinic crystal phase of Cu$_3$V$_2$O$_8$ is in the RPOM–CV2 composite (JCPDS No: 74-1503).[48] It also reveals that proper growth of Cu$_3$V$_2$O$_8$ nanoparticles occurs on the RGO nanosheets in the presence of POM. Moreover, the crystallite size of CV in the RPOM–CV2 composite was calculated to be 6.3 Å by considering the most intense peak at 32.2° according to the Debye–Scherrer equation. Similarly, the XRD patterns of the RPOM–CV3 composite were consistent with those of bare CV and RPOM, showing a resemblance with that of the precursor and verifying the composite formation (Fig. S1, ESI†).

### 3.2. Raman spectroscopic analysis

Raman spectroscopy is an important spectroscopic technique used to investigate the various vibrational modes present in molecules. The presence of vibrational modes of both pristine metal vanadates and the D and G bands of RGO in the Raman spectra of the as-synthesized nanocomposites provides successful evidence in favor of composite formation. Fig. 2a portrays the Raman spectra of the RPOM, RPOM–AV2, and RPOM–CV2 composites. In the case of RPOM, the D-band at 1353.9 cm$^{-1}$ arises owing to the out-of-plane vibrations of sp$^3$ hybridized carbon atoms in RGO, whereas the G-band at 1593.8 cm$^{-1}$ corresponds to the vibration modes of the in-plane vibrations of sp$^2$ hybridized carbon atoms of RGO (Fig. 2a).[49–51] In the case of pristine AV, the characteristic Raman peaks at 532 cm$^{-1}$ corresponding to the V–O–V stretching vibrations (Fig. S2a, ESI†) are shifted to 490 cm$^{-1}$ after composite formation with RPOM. Peaks at 877 and 922 cm$^{-1}$, which are attributed to V–O–Ag and V=O stretching vibrations, are shifted to 878.7 cm$^{-1}$ and 917.2 cm$^{-1}$ due to the interaction of RPOM with AV, respectively.[52] Moreover, the peaks at 1353.9 cm$^{-1}$ and 1583.3 cm$^{-1}$ are attributed to the presence of D and G bands of RPOM, respectively. The peaks at 799.8 cm$^{-1}$, 857.8, and 908.9 cm$^{-1}$ corresponding to the vibrations of the VO$_3$ units shift to 800.6 cm$^{-1}$, 852.4 cm$^{-1}$, and 905.1 cm$^{-1}$ owing to the strong interaction of RPOM with CV, respectively (Fig. S2b, ESI†).[53] Moreover, the peaks at 1353.9 cm$^{-1}$ and 1583.3 cm$^{-1}$ are attributed to the presence of D and G bands of RGO in RPOM–CV composites, respectively. Similarly, the Raman spectra of the higher-loaded RPOM–AV3 (bare AV) and RPOM–CV3 (bare CV) composites exhibit a pattern comparable to that observed for RPOM–AV2 and RPOM–CV2, respectively (Fig. S2, ESI†).

Interestingly, it has been observed that although there was no shift in the position of the D-band of pristine RPOM after
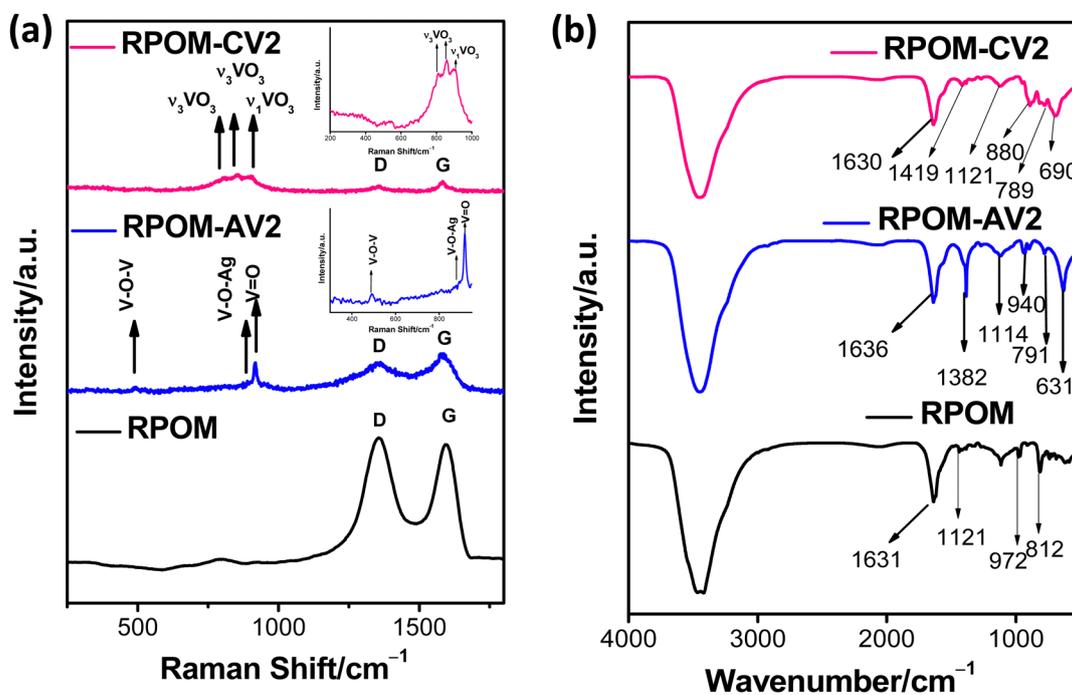


**Fig. 2** (a) Raman spectra of RPOM, RPOM–AV2, and RPOM–CV2 composites (inset: Raman spectra of composites in the range of 300 cm$^{-1}$ –1000 cm$^{-1}$). (b) FT-IR spectra of RPOM, RPOM–AV2 and RPOM–CV2 composites.

composite formation with the metal vanadates, a significant blue shift in the position of the G-band occurred from 1593.8 cm$^{-1}$ to 1583.3 cm$^{-1}$ after composite formation in both cases. This may be due to the interaction of RPOM with the metal vanadates, which affects the in-plane vibrations of the C=C bonds in RGO. In addition, the crystallite size of the composites can be calculated from the Tuinstra–Koenig eqn (3) by considering the ratio of the intensities of the D-band ($I_D$) and G-band ($I_G$).[54]

$$L_\alpha = 2.4 \times 10^{-10}\lambda^4\left(\frac{I_D}{I_G}\right)^{-1}, \qquad (3)$$

where the crystallite size is represented by $L_\alpha$ and $\lambda$ denotes the wavelength of the laser beam in nm. The $I_D/I_G$ ratio decreases from 1.04 in RPOM to 0.83 and 0.86 after composite formation with AV and CV, respectively. This leads to an increase in the average crystallite size from 16.1 nm in RPOM to 20.2 nm and 19.5 nm in the RPOM–AV and RPOM–CV composites, respectively. Therefore, the interaction of RPOM with the metal vanadates results in an increase in the crystallite size of the composites, which boosts electron–hole separation, thereby enhancing the photocatalytic performance of the as-synthesized composites.

### 3.3.   FT-IR analysis

FT-IR analysis was carried out to monitor the changes in the stretching and bending vibrations of the metal vanadates after nanocomposite formation. Fig. 2b shows that in the case of RPOM, the peaks at 613 cm$^{-1}$ and 812 cm$^{-1}$ correspond to the stretching vibrations of the bridging W–O–W units, and the peak at 972 cm$^{-1}$ arises due to the stretching vibration of the terminal W–O bond of the Lindqvist POM.[55] Moreover, the peak at 1121 cm$^{-1}$ corresponds to the C–O epoxy stretching vibrations of RGO.[56] Fig. S3 (ESI†) depicts the FT-IR spectra of pristine AV and CV. In the case of bare AV, the peaks at 649.1 cm$^{-1}$ and 775.6 cm$^{-1}$, which arise due to the anti-symmetric stretching vibrations of VO$_3$ units, are shifted to 630.8 cm$^{-1}$ and 791.3 cm$^{-1}$, respectively, owing to the inter-action of RPOM with AV. The peak at 934.6 cm$^{-1}$ for pristine AV is attributed to the symmetric stretching vibrations of VO$_3$ units. A red shift in this peak's position to 939.8 cm$^{-1}$ has been observed for RPOM–AV2 after composite formation as a result of the strong interaction of AV with RPOM.[57] The peak at 1388 cm$^{-1}$ for both pristine AV and RPOM–AV2 indicates the presence of N=O bending vibrations of nitro groups of pre-cursors AgNO$_3$.[58] Moreover, the peaks at 1114.4 cm$^{-1}$ and 1382.3 cm$^{-1}$ in RPOM–AV2 composites correspond to C–O stretching and O–H deformation vibrations of RGO, respectively.[59] In the case of RPOM–CV2 composites, the $\delta_{Cu–OH}$ deformation vibrations at 1116.3 cm$^{-1}$ for pristine CV shift slightly to 1121.6 cm$^{-1}$ owing to the strong interaction of CV with RPOM. Peaks at 891.2 cm$^{-1}$ and 795.1 cm$^{-1}$, which arise owing to the symmetric and anti-symmetric stretching vibrations of VO$_3$ units, respectively, in pristine CV, shift to 880.2 cm$^{-1}$ and 789.3 cm$^{-1}$ after nanocomposite formation

with RPOM, respectively. Similarly, the peak at 697.3 cm$^{-1}$, which is attributed to Cu–O bending vibration, also shifts to 689.9 cm$^{-1}$ for the RPOM–CV2 nanocomposites because of the strong chemical interaction of RPOM with CV. The peak at 1412.4 cm$^{-1}$ for bare CV, which is attributed to the presence of overtones or combination bands, shifts to 1419.3 cm$^{-1}$ after composite formation with RPOM.[60,61]

### 3.4.   Optical and thermal properties

The UV-DRS spectra of various samples were taken in the solid phase using a UV-visible spectrophotometer. It was found that the absorbance range of bare AV was near the UV-visible region, *i.e.*, from 250 to 500 nm, with the absorbance peak at 381 nm. Similarly, the absorbance range for bare CV was also near the UV-visible region from 230 nm to 660 nm, with the absorbance peak at 361 nm. The absorbance peak of RPOM was also taken, showing absorption in the visible to near-infrared region, *i.e.*, from 230 to 1100 nm (Fig. S4, ESI†). The band gap ($E_g$) calculation was conducted with the Tauc plot; the band gaps were obtained using direct and indirect methods. The band gap energy for bare AV was 2.6 eV using the direct method. Similarly, the band gap energy for pristine CV was 1.6 eV using the direct method. Moreover, the band gap energy for bare RPOM was 0.9 eV using the direct method.

The absorbance spectra of the RPOM–AV2 and RPOM–CV2 composites were also obtained using a UV-DRS spectroph-ometer. The absorbance ranges for RPOM–AV2 and RPOM–AV3 were within UV to the initially visible region, *i.e.*, 230 to 500 nm, corresponding to the bare AV absorbance spectra. The absor-bance range for RPOM–CV2 and RPOM–CV3 was within the UV to the visible region, *i.e.*, 230 to 660 nm, corresponding to the CV absorbance spectra (Fig. S4, ESI†). The band gap calculation was conducted with the Tauc plot, and the band gaps were obtained using direct methods. The band gap energies for RPOM–AV2 and RPOM–AV3 were 2.0 eV and 2.48 eV with the direct method, respectively (Fig. S5, ESI†). Similarly, the band gap energies for RPOM–CV2 and RPOM–CV3 were 1.5 eV and 1.43 eV using the direct method, respectively (Fig. S5, ESI†). This study conveys that there is a decrease in the band gap energy for the composites, *i.e.*, RPOM–AV2, RPOM–AV3, RPOM–CV2, and RPOM–CV3, compared to the precursor, *i.e.*, pristine AV, CV, and RPOM. This could be attributed to the transition in doped impurities and defects caused by silver vanadate and copper vanadate on POM containing reduced graphene oxide. The decrease in the band gap energy of the hybrid RPOM–AV and RPOM–CV composites is because of the electronic interaction of individual precursors, thus modifying the band structure of the composites.

The TGA curve depicts that the pristine metal vanadates exhibit excellent thermal stability with mass losses of only 3.6% and 1.3% of pristine AV and CV, respectively, at a temperature of 500 °C (Fig. S6a, ESI†). However, RPOM shows a 15% mass loss at 500 °C owing to the pyrolysis of oxygen-containing functionalities of RGO (Fig. S6b, ESI†).[62] RPOM–AV2 and RPOM–CV2 exhibit mass losses of 11% and 9%, respectively, at that temperature. This reveals that the introduction of

pristine metal vanadates to RPOM increases the thermal stability of the as-synthesized nanocomposites.

### 3.5.  Photoluminescence spectral studies

Photoluminescence (PL) spectroscopy provides insight into the radiative recombination processes of the photogenerated charge carriers. As depicted in Fig. S7 (ESI†), the emission peak for the pristine metal vanadates and the composites arises at 430 nm owing to the recombination of electrons from the conduction band and the holes in the valence band in the case of vanadates.[63] For RPOM, a broad emission peak at 445 nm appears owing to electron–hole recombination in RGO.[64] It is observed that the PL intensity of the bare metal vanadates is reduced after composite formation with RPOM. This suggests that the incorporation of RPOM into pristine metal vanadates facilitates charge transfer and reduces the rate of electron–hole recombination in the RPOM–AV2 and RPOM–CV2 composites.

### 3.6.  Morphological studies and surface properties

The morphology and elemental distribution of the as-synthesized composites are investigated using FESEM. The FESEM images of RPOM–AV2 reveal that $AgVO_3$ nanorods of average width of 100–200 nm and length of 1–2 μm are formed on RGO nanosheets through co-precipitation (Fig. 3a and b). Fig. S3c–h (ESI†) represents the EDS elemental mapping for C, O, P, Ag, V, and W, denoting that the RPOM–AV2 composites are successfully synthesized. Similarly, the FESEM image and

EDS elemental mapping of RPOM–AV3 substantiate the composite formation (Fig. S8a–h, ESI†). For the RPOM–CV2 composites, the FESEM images reveal the uniform distribution of spherical CV nanoparticles with an average diameter of ∼50–200 nm on the RGO nanosheets (Fig. 3i and j). Moreover, the corresponding EDS elemental mapping for C, O, P, Cu, V, and W indicates the successful formation of the RPOM–CV2 composites (Fig. 3k–p). Further, FESEM and EDS elemental mapping of RPOM–CV3 validates the composite formation (Fig. S8i–p, ESI†). Fig. S9(a)–(e) (ESI†) represents the FESEM image and the corresponding energy-dispersive X-ray spectroscopy (EDS) elemental mapping of pristine RPOM.

The microstructural analysis of the as-synthesized composites is further carried out in detail with the help of TEM and HRTEM imaging. In the case of the RPOM–AV2 composites, the TEM images reveal that metallic Ag nanoparticles decorated with $AgVO_3$ nanorods are formed on RGO nanosheets (Fig. 4a and b). The TEM image for bare AV reveals that metallic Ag nanoparticles with a diameter of 18 nm are anchored on 1D $AgVO_3$ nanorods with an average width of ∼180 nm and ∼1.3 μm in length, as portrayed in Fig. S10 (ESI†). The HRTEM image reveals the presence of five sets of lattice fringes, corresponding to the presence of the (111), (240), (150), (222), and (−310) planes of α-$AgVO_3$ (Fig. 4c). The SAED pattern portrays the single crystalline nature of the $AgVO_3$ nanorods. Moreover, the diffraction rings observed in the SAED pattern reveal the presence of the (240) and (111) planes of monoclinic
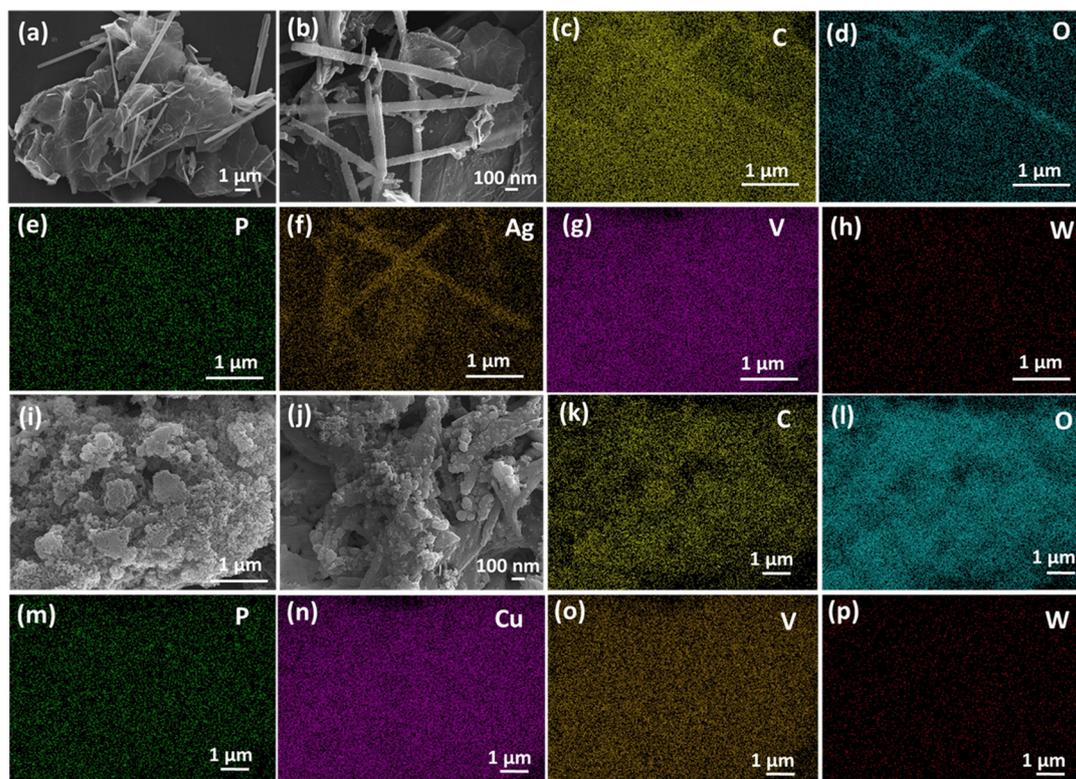


Fig. 3    FESEM images of RPOM−AV2 at (a) lower and (b) higher magnifications, EDX elemental mapping for (c) C, (d) O, (e) P, (f) Ag, (g) V, (h) and W. (i) and (j) FESEM images of RPOM−CV2. EDX elemental mapping for (k) C, (l) O, (m) P, (n) Cu, (o) V, and (p) W.
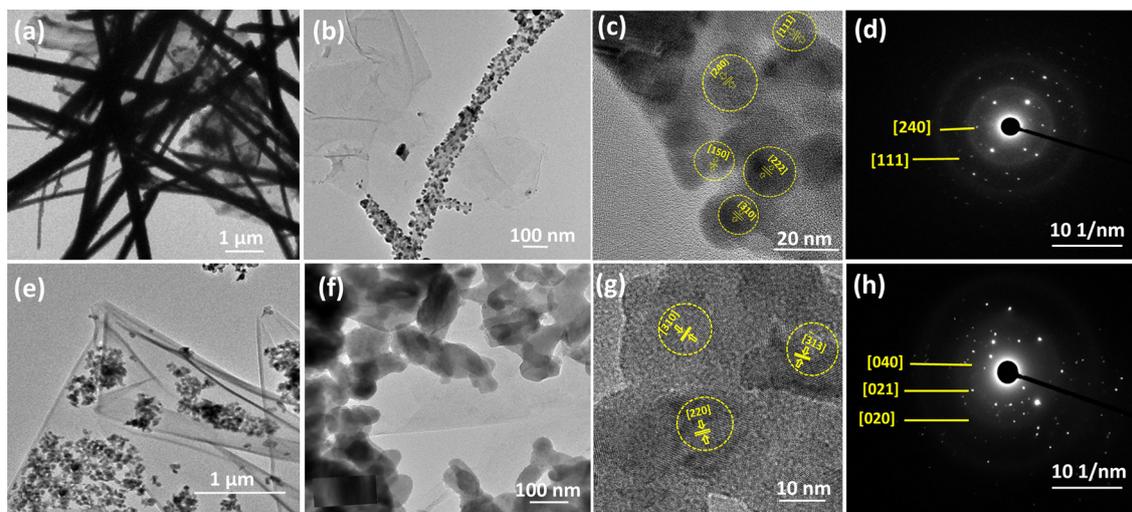
Fig. 4 TEM images of RPOM–AV2 at (a) lower and (b) higher magnifications. (c) HRTEM image. (d) SAED pattern of RPOM–AV2 and TEM images of RPOM–CV2 at (e) lower and (f) higher magnifications. (g) HRTEM image. (h) SAED pattern of RPOM–CV2.

α-AgVO$_3$ (Fig. 4d). The TEM image of the lower and higher magnifications of RPOM–AV3 is shown in Fig. S11a and b (ESI†). The HRTEM image reveals the presence of a lattice fringe corresponding to the (−131) plane of α-AgVO$_3$ (Fig. S11c, ESI†). The SAED pattern showed the presence of the (−131) plane of monoclinic α-AgVO$_3$ (Fig. S11d, ESI†).

The TEM images of RPOM–CV2 composites confirm the uniform distribution of spherical CV nanoparticles with an average diameter of ∼90 nm on the RGO nanosheets (Fig. 4e and f). The HRTEM image of the RPOM–CV2 composites reveals the presence of crystal lattice fringes corresponding to the (310), (220), and (−313) planes of the monoclinic CV (Fig. 4g). Additionally, the diffraction rings observed in the SAED pattern reveal the presence of the (021), (040), and (020) planes of the monoclinic CV (Fig. 4h). Fig. S11e and f (ESI†) show the TEM images of RPOM–CV3 at low and higher magnifications. The HRTEM images reveal that the lattice fringe corresponds to the (012) crystallographic plane of the monoclinic CV (Fig. S11g, ESI†). The SAED pattern further confirms the presence of (012) planes in the monoclinic CV (Fig. S11h, ESI†).

The specific surface area of composites is determined with the help of the Brunauer–Emmett–Teller (BET) equation through the adsorption and desorption of N$_2$ gas. The mesoporosity of the materials has been confirmed from the type-IV hysteresis loop, as observed in Fig. S12(a)–(c) (ESI†).[65] The specific surface area of RPOM–AV composites is 86.7 m$^2$ g$^{-1}$, which is almost 6 times higher than that of RPOM (13.7 m$^2$ g$^{-1}$). Moreover, the specific surface area of the RPOM–CV composites is 20.5 m$^2$ g$^{-1}$, which is slightly higher than that of RPOM. In addition, the pore volumes of RPOM–AV and RPOM–CV are 0.52 cc g$^{-1}$ and 0.08 cc g$^{-1}$, respectively, which are also greater than that of RPOM (0.02 cc g$^{-1}$). Therefore, composite formation with metal vanadates increases the specific surface area with a higher pore volume and abundant active sites, which

ultimately causes an enhancement in the photocatalytic performance of the as-synthesized composites.

X-Ray photoelectron spectroscopy measurements were performed to determine the surface chemical composition and oxidation states of the constituent elements present in the composites. The survey spectra depicted in Fig. S13a and b (ESI†) reveal the presence of Ag, V, O, C, W and Cu, V, O, C, W in the RPOM–AV and RPOM–CV composites, respectively. The Ag 3d core level spectra are fitted with two doublet peaks at binding energies of 367.5 and 373.5 eV, corresponding to 3d$_{5/2}$ and 3d$_{3/2}$ lineshapes in pristine AgVO$_3$, which confirms the presence of Ag$^+$ oxidation state, respectively.[21,22] However, after composite formation, both peaks shift to slightly higher binding energies at 368.1 and 373.9 eV owing to the interaction of AV with RGO and POM (Fig. S14a, ESI†). Fig. S14b (ESI†) depicts the V 2p core level spectra. The characteristic peaks in the V 2p lineshape at binding energies of 516.9 eV and 524.1 eV are attributed to the 2p$_{5/2}$ and 2p$_{3/2}$ lineshapes, indicating the presence of V in the +5 oxidation state in pristine AV, respectively.[24,25] Moreover, the peak arising at 2p$_{5/2}$ is further resolved into a doublet signal at binding energies of 516.5 and 517.4 eV, which are slightly shifted to lower binding energies at 516.2 eV and 517.3 eV, respectively. However, a red shift in the binding energies is observed in the case of 2p$_{3/2}$ signal from 524.1 eV in bare AV to 524.9 eV owing to composite formation. The O 1s lineshape is further fitted with peaks at binding energies at 529.9 eV and 531.6 eV, which correspond to the presence of lattice O atoms and surface adsorbed O atoms, respectively, in pristine AV (Fig. S14c, ESI†).[21] These peaks are further shifted to 530.7 and 532.6 eV, respectively, owing to electron-cloud redistribution between AV and POM with RGO serving as electron-mediator. The C 1s spectrum is further fitted with three peaks at 284.7, 285.4 and 286.6 eV, which further correspond to the presence of graphitic carbon, C–O and C–OH functional groups of RGO, respectively, in the

RPOM–AV composites, as illustrated in Fig. S14d (ESI†).[33,35] The W 4f core level spectra are fitted with two peaks at binding energies of 36.1 and 38.2 eV, which correspond to $4f_{7/2}$ and $4f_{5/2}$, signifying the presence of W in +6 oxidation state (Fig. S14e, ESI†).[66]

In the case of RPOM–CV composites, the Cu 2p core level spectra are fitted with characteristic peaks, which correspond to the presence of $2p_{1/2}$ and $2p_{3/2}$ states, thereby confirming the +2 valency of Cu.[20,23] The $2p_{3/2}$ lineshape is further fitted with doublet peaks at binding energies of 930.6 and 932.9 eV in the pristine CV, which slightly shift to lower binding energies at 930.4 eV and 932.6 eV. A similar trend in the red shift of binding energies is also observed in the Cu $2p_{1/2}$ lineshape after composite formation. This suggests that there is an increase in electron density after composite formation owing to the flow of electrons from POM to CV through RGO serving as the electron mediator, as observed from the charge transfer mechanism depicted in Fig. S15a (ESI†). The V 2p lineshape is further resolved into two peaks at binding energies of 515.1 eV and 522.4 eV, which are attributed to the $3d_{5/2}$ and $3d_{3/2}$ lineshapes in pristine CV and confirm the presence of V in the +5 oxidation state, respectively.[26,48] There is a slight shift in binding energies to lower values by 0.2 eV after composite formation, as depicted in Fig. S15b (ESI†). Moreover, the O 1s lineshape is fitted with a triplet signal at binding energies of 284.8 eV and 285.8 eV, corresponding to the presence of lattice and surface adsorbed O atoms in pristine CV, as shown in Fig. S15c (ESI†). Moreover, there was no significant shift in the binding energies of these peaks after RPOM–CV composite formation. Fig. S15d (ESI†) illustrates the C 1s core level spectrum, which is further fitted with two peaks at 284.8 eV and 285.8 eV owing to the presence of graphitic carbon and C–O groups of RGO, respectively.[33,35] The W 4f core level spectra are further fitted with peaks arising at binding energy representing $4f_{5/2}$, which also signifies the presence of W in the +6 oxidation state, as depicted in Fig. S15e (ESI†).[66]

### 3.7. Photoelectrochemical measurements

The photoresponse of the as-synthesized composites was recorded by carrying out the current *versus* voltage measurements in the presence of light irradiation. The photocurrent density of the heterostructures increases after the formation of the RPOM–AV and RPOM–CV composites, as portrayed in Fig. 5a and d. Among the as-synthesized composites with different loading variations, the highest photocurrent density is observed for RPOM–AV2 composites ($\sim$223.7 µA cm$^{-2}$), which is 51-fold higher in comparison with pristine AV ($\sim$4.4 µA cm$^{-2}$). Similarly, in the case of copper vanadates, it was observed that the introduction of RPOM to CV enhances the photoresponse of the as-synthesized RPOM–CV composites. Among the RPOM–CV composites with different loading variations, the greatest photocurrent density ($\sim$85.8 µA cm$^{-2}$) was observed for the RPOM–CV2 composites, which is 6 times higher in comparison with pristine CV ($\sim$14.6 µA cm$^{-2}$). Fig. S16a and b (ESI†) portray that the current densities of

RGO–AV (23.1 µA cm$^{-2}$) and RGO–CV (33.6 µA cm$^{-2}$) are much less than that of RPOM–AV2 and RPOM–CV2 composites. This indicates that the polyoxometalates may serve as cocatalysts and play a crucial role in enhancing the photoelectrochemical performance. Moreover, the photocurrent densities of AV–POM (19.4 µA cm$^{-2}$) and CV–POM (8.5 µA cm$^{-2}$) are also much lower compared to the RPOM–AV and RPOM–CV composites, respectively (Fig. S16a and b, ESI†). This also reveals that RGO enhances the charge transfer between metal vanadates and POM and boosts charge carrier separation, which in turn leads to an augmentation of the photoelectrochemical performance of the as-synthesized composites. Transient photocurrent spectra were recorded under chopped dark and illumination conditions at a regular interval of 20 seconds to determine the photostability of the as-synthesized composites. It can be noted that the as-synthesized composites of both silver and copper vanadates with RPOM are fairly stable and durable against photo-corrosion (Fig. 5b and e). No decrease in the photocurrent density was observed for 260 seconds, which indicated the photostability of the nanocomposites. To develop a better understanding of the interfacial charge transmission processes, impedance analysis was carried out in the presence of light.

The Nyquist plots of the RPOM–AV composites revealed that the charge transfer resistance of RPOM–AV2 was 312.4 Ω, which was significantly lower compared to pristine AV (11.3 kΩ) and RPOM (5.5 kΩ), thereby ensuring facile charge transfer (Fig. 5c). Moreover, it was observed that there was a significant reduction in the charge transfer resistance of RPOM–CV2 composites (382.8 Ω) in comparison with pure CV (18.9 kΩ), as shown in Fig. 5f. Because RPOM–AV2 and RPOM–CV2 exhibit the highest photocurrent density among the as-synthesized RPOM–AV and RPOM–CV composites, they are considered for further study (Table S1, ESI†). Furthermore, the charge carrier lifetime was calculated using Bode plot analysis. It is observed that the charge carrier lifetime increases after composite formation compared to pristine RPOM. The charge carrier lifetime for RPOM–AV2 (3.9 ms) is much higher than that for pristine RPOM (0.3 ms) and AV (0.2 ms), indicating a lower rate of electron–hole recombination (Fig. S17a, ESI†). In the case of pristine CV, the charge carrier lifetime is 3.2 ms, while it is 1.3 ms for RPOM–CV composites, as observed from Fig. S17b (ESI†). Therefore, it can be noted that the charge carrier lifetime of the composites increases after the incorporation of CV into RPOM. The higher lifetime of the charge carriers leads to superior photocatalytic performance after composite formation compared to bare RPOM.

To explore the electrochemical properties of the semiconductor photoelectrodes, a Mott–Schottky analysis was carried out. All the semiconductors exhibit a positive slope, which confirms n-type semiconductivity.[67,68] The flat-band potentials ($E_{fb}$) of RPOM, RPOM–AV2, and RPOM–CV2 are −0.43 V, −0.52 V, and −0.46 V, respectively, as shown in Fig. 6. It is observed that the flat-band potentials of RPOM–AV2 and RPOM–CV2 composites are more negative than that of RPOM. Table 1 presents the various electrochemical parameters
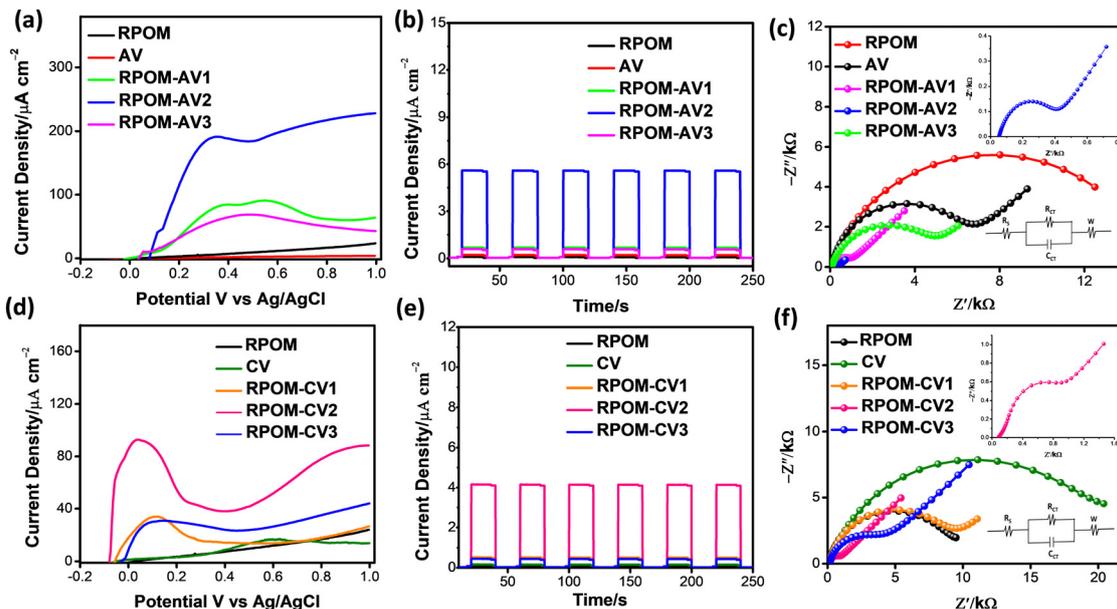
Fig. 5 (a) Current *versus* voltage curve. (b) Transient photocurrent. (c) Nyquist plots of RPOM−AV composites (inset: Nyquist plot of RPOM−AV2). (d) Current *versus* voltage curve. (e) Transient photocurrent. (f) Nyquist plots of RPOM−CV composites (inset: Nyquist plot of RPOM−CV2).
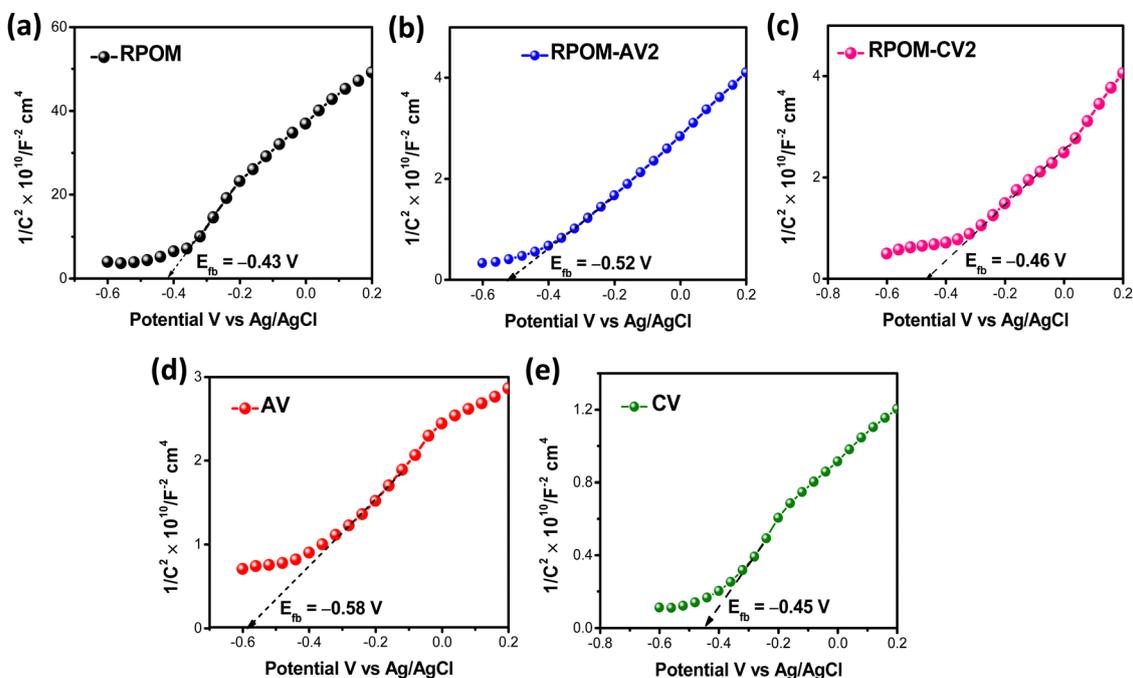


Fig. 6 Mott−Schottky plots of (a) RPOM, (b) RPOM−AV2, (c) RPOM−CV2, (d) pristine AV and (e) pristine CV.

derived from the Mott–Schottky plots of the pristine materials as well as their composites.

Moreover, the donor density ($N_d$) of the RPOM–AV2 and RPOM–CV2 composites is much higher than that of RPOM and pristine metal vanadates. The donor densities of RPOM–AV2 ($17.1 \times 10^{17}$ cm$^{-3}$) and RPOM–CV2 ($20.1 \times 10^{16}$ cm$^{-3}$) are 7 times and 3 times higher compared to pristine AV

($2.4 \times 10^{17}$ cm$^{-3}$) and CV ($6.7 \times 10^{16}$ cm$^{-3}$), respectively, which ultimately leads to a significant enhancement in the photocurrent density of the composites in comparison with the metal vanadates, as observed from the linear sweep voltammogram. Fig. S18 (ESI†) shows the variation in the width of the space charge region as a function of the applied potential. There is a significant decrease in the width of the space charge region of

**Table 1** Electrochemical parameters determined from the Mott−Schottky plots of AV, CV, RPOM, RPOM−AV2, and RPOM−CV2 composites

| Material | $E_{fb}$ vs. Ag/AgCl (V) | $E_{fb}$ vs. RHE (V) | CB (eV) | $E_g$ (eV) | VB (eV) | $N_d$ (cm$^{-3}$) |
|---|---|---|---|---|---|---|
| AV | −0.58 | 0.03 | −0.17 | 2.6 | 2.4 | $2.4 \times 10^{17}$ |
| CV | −0.45 | 0.16 | −0.04 | 1.6 | 1.56 | $6.7 \times 10^{16}$ |
| RPOM | −0.43 | 0.18 | −0.02 | 0.9 | 0.88 | $11.9 \times 10^{16}$ |
| RPOM−AV2 | −0.52 | 0.09 | — | — | — | $17.1 \times 10^{17}$ |
| RPOM−CV2 | −0.46 | 0.15 | — | — | — | $20.1 \times 10^{16}$ |

the composites compared to the pristine metal vanadates, which facilitates interfacial charge transfer after composite formation with RPOM.

### 3.8. Rose bengal (RB) and methylene blue (MB) degradation

The RB degradation was conducted using RPOM−AV3 composite material. A solution of 50 μM RB dye with 0.01 mg mL$^{-1}$ of RPOM−AV3 was used to study the degradation of RB. It was noticed that the RB degradation occurred in the absence of light, and the dye was adsorbed on the catalyst surface owing to the broad surface area of RPOM−AV composites. The reaction mixture remained heterogeneous after dye adsorption; hence, the solution was centrifuged to separate the catalyst. The major absorption peak at 548 nm for the RB solution observed in UV-vis spectra arises because of the π to π* transition (Fig. 7a).[69] The RB degradation was tested with the precursor materials RPOM and AV. The precursor RPOM showed negligible RB degradation, and AV showed 68% RB absorption within 2 h when applied to RB dye (Fig. 7b). Further, a time-dependent degradation study of RB with the RPOM−AV3 catalyst was performed at varying times. A steady increase in the adsorption was noted in the period from 0, 20, 40, 60, 80, 100, and 120 min.

The adsorption efficiency after 120 minutes was 94% ± 0.03% (Fig. 7a (inset)). Additionally, to check the recyclability of the catalysts, the catalytic activity of RPOM−AV3 was tested through several cycles for the removal of RB, as shown in Fig. 7c. It was observed that there was no appreciable loss in the degradation efficiency of the as-synthesized composites towards RB adsorption even after 3 cycle runs. The RPOM−AV3 surface initially had unoccupied active sites. As the active sites become exhausted, the adsorption process becomes less effective. The study demonstrates that the synergistic interaction between RPOM and AV in the RPOM−AV3 composite enhances the dye removal process and reaches a point of saturation after 120 min. The RPOM−AV2 composite was applied for the RB dye adsorption but, in contrast, exhibited a lower dye removal process compared to RPOM−AV3. The dye removal efficiency was 49% after 120 min (Fig. S19a, ESI†).

RPOM−CV3 was used as a photocatalyst to perform the MB dye degradation in the presence of 112 W visible light. This hybrid composite did not show any discernible degradation of MB dye in the dark when stirred for 1 hour; thus, the adsorption–desorption equilibrium was maintained. The absorption peak of MB observed at 664 nm corresponds to the (–N═C═)
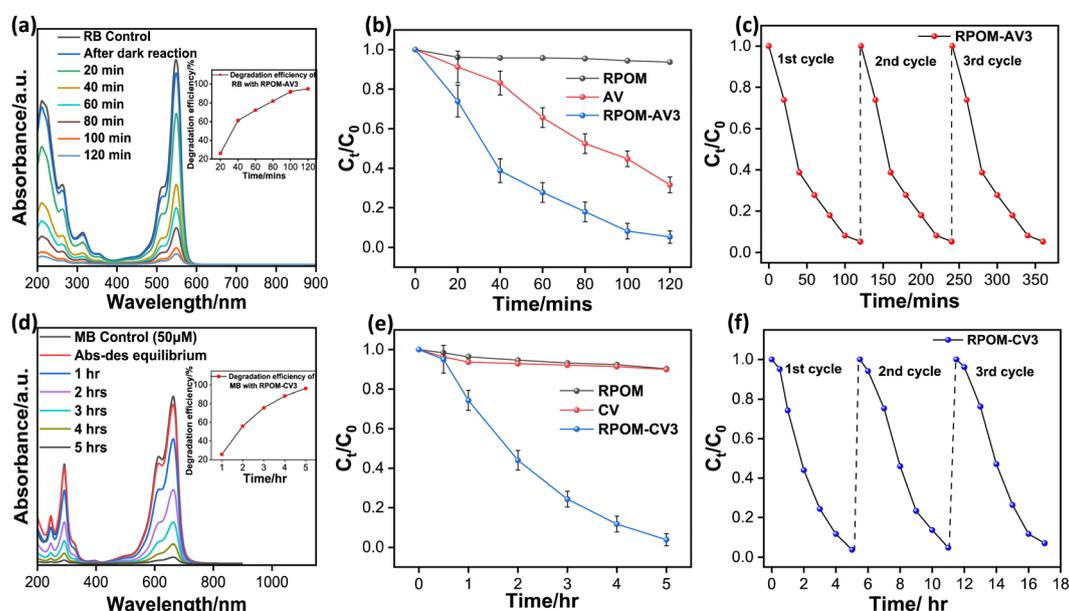


**Fig. 7** (a) UV-Visible absorption spectra for the adsorption of RB dye (inset: degradation efficiency of RB dye in the presence of RPOM−AV3 composites). (b) Adsorption of RB using RPOM, AV and RPOM−AV3. (c) Recyclability of RPOM−AV3 after successive cycles of RB absorption. (d) UV-Visible absorption spectra for photocatalytic degradation of MB dye (inset: degradation efficiency of MB dye in the presence of RPOM−CV3 composites). (e) Degradation of MB using RPOM, CV, and RPOM−CV3. (f) Recyclability of RPOM−CV3 after successive cycles of MB degradation.

iminium part of MB.[70,71] The UV-visible spectra of MB degradation were examined under variable periods from 0 to 5 h, as shown in Fig. 7d. The photocatalytic degradation of MB was evaluated using the precursor RPOM and CV. These results indicate that the precursor RPOM and CV have a limited effect on photocatalytic MB degradation. The MB degradation efficiency with respect to time is shown in Fig. 7d (inset). After 5 h of photocatalytic degradation of MB dye, the degradation efficiency was 96% ± 0.04%. The degradation of MB dye is due to the generation of adequate holes/radicals after the photon absorption by photocatalyst RPOM–CV3. The MB dye is adsorbed on the active site of the surface of the photocatalyst. The photo-generated holes/radicals consequently degrade the MB dye. The UV-vis spectra of MB using precursor RPOM and CV exhibited minimal photocatalytic degradation of MB (Fig. 7e). Furthermore, to assess the recyclability, the catalytic performance of RPOM–CV3 was evaluated over multiple cycles for the removal of MB, as depicted in Fig. 7f. The result indicated that the degradation efficiency of the synthesized RPOM–CV3 composites for MB degradation remained constant, with no significant decrease in performance even after 3 successive cycles. The study indicates that the RPOM–CV3 composite exhibits elevated dye degradation capability owing to the cooperative effect between RPOM and CV. The photocatalytic degradation proceeds according to a pseudo-first-order with a 0.011 min$^{-1}$ reaction rate at a pH of 6.3. The RPOM–CV2 composite was employed for the MB degradation, but it showed low dye degradation efficiency relative to the RPOM–CV3. The dye degradation efficiency was quantified to be 79% after 5 h (Fig. S19b, ESI†). A comparative study of MB degradation using different photocatalysts is presented in Table S2 (ESI†).

In this study, we investigated the role of photo-induced reactive species crucial for the photocatalytic process, namely electrons, holes, and hydroxyl radicals. Photocatalytic dye degradation has been performed with a series of scavengers: ethylenediaminetetraacetic acid disodium salt hydrate (EDTA) to scavenge h$^+$, silver nitrate (AgNO$_3$) to scavenge e$^-$, and isopropyl alcohol (IPA) to scavenge hydroxyl radicals ($^\bullet$OH). The MB degradation utilizing quenchers over the photocatalyst RPOM–CV3 when exposed to visible light irradiation is illustrated in Fig. S20 (ESI†). On adding IPA (1 mmol L$^{-1}$), the degradation of MB is inhibited, indicating that $^\bullet$OH radical species were required for dye elimination. The degradation was slightly enhanced upon the addition of AgNO$_3$ (1 mmol L$^{-1}$), indicating that e$^-$ presence is less prominent for dye degradation. The addition of EDTA (1 mmol L$^{-1}$) to the reaction mixture shows that the degradation of MB dye is more enhanced, indicating that h$^+$ radicals are also not prominent; thus, the absence of h$^+$ rather increases the dye removal process. Therefore, the presence of $^\bullet$OH radical species is notable for dye degradation.
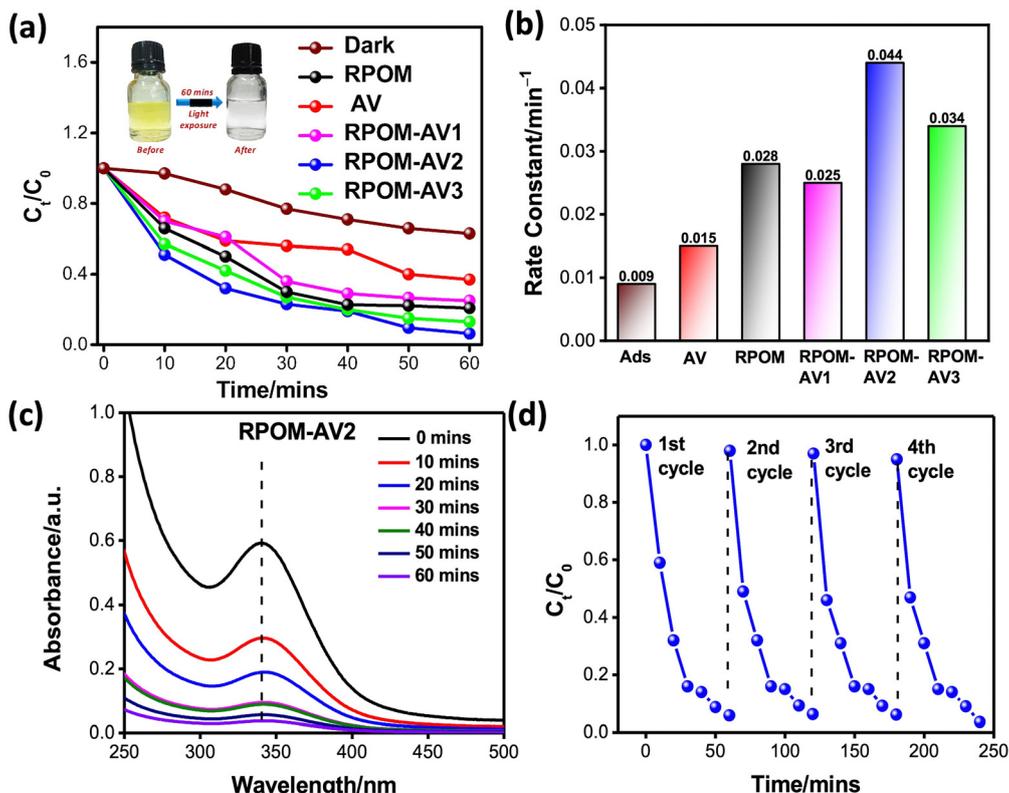
### 3.9. Photocatalytic Cr(VI) reduction

The photocatalytic activity of the RPOM–AV2 composite was examined by following the rate of photocatalytic reduction of toxic Cr(VI) to non-toxic Cr(III) under visible light. It was observed that the removal efficiency of hexavalent Cr(VI) was only 36% under the dark for 60 minutes owing to adsorption (Fig. 8a). It was observed that the concentration of toxic Cr(VI) gradually decreased with time and the effective photocatalytic removal of toxic Cr(VI) up to 94% was observed in 60 minutes under visible light illumination at acidic pH (pH = 2) using RPOM–AV2 nanocomposite as photocatalyst in the presence of 8 vol% of isopropanol as a sacrificial agent, while pristine AV exhibited 63% removal efficiency of Cr(VI) under similar reaction conditions. Fig. 8b depicts the rate constants for the photoreduction of Cr(VI) using pristine AV, RPOM, and RPOM–AV composites with various loading variations. Among the as-synthesized RPOM–AV composites, RPOM–AV2 exhibits the highest rate of photocatalytic Cr(VI) reduction with a rate constant of 0.044 min$^{-1}$ (pseudo-first order reaction). It was observed that by further increasing the metal loading concentration on RPOM, there was a decrease in the kinetic rate constants for photocatalytic Cr(VI) reduction, as observed in Table S3 and Fig. S21a (ESI†). Fig. 8c illustrates the UV-visible absorption spectra of 100 ppm Cr(VI) solutions treated with the RPOM–AV2 composite. It was observed that the strong absorption of Cr(VI) at 340 nm decreased with time, and almost no absorption occurred after 60 minutes of light irradiation. Moreover, it was noticed that the efficiency of Cr(VI) reduction was almost 74% when using the RGO–AV composite, which increased to 94% with the RPOM–AV2 composite, as shown in Fig. S21b (ESI†). This reflects the role of POM in enhancing the photocatalytic performance of the as-synthesized composites. The effect of hole scavengers, i.e., EDTA and isopropanol, on the rate of photocatalytic Cr(VI) reduction is presented in Fig. S21c (ESI†). It was observed that without using a sacrificial agent, the photocatalytic Cr(VI) reduction efficiency for RPOM–AV composites was 65% after 60 minutes, while it reached 72% and 94% in the presence of EDTA and isopropanol, respectively. The sacrificial agent captures the holes, which reduces electron–hole recombination and increases the photocatalytic performance of the as-synthesized composites. Moreover, to check the reusability and stability of the catalysts, the catalytic activity of the RPOM–AV composites was tested through several cycles for the removal of hexavalent Cr(VI), as shown in Fig. 8d. It was observed that there was no appreciable loss in the degradation efficiency of the as-synthesized composites towards photocatalytic Cr(VI) reduction even after several cyclic runs. Table S4 (ESI†) presents a comparative study of the photocatalytic activity of various metal vanadate-based composites towards Cr(VI) reduction from where the as-synthesized RPOM-based silver vanadate composites exhibit much superior performance.[72–77]

The photocatalytic removal of Cr(VI) was also performed with the help of the RPOM–CV composites. However, the results were not at all encouraging, as only 13% removal of Cr(VI) was observed after 60 minutes, as shown in Fig. S21d (ESI†). Copper vanadate-based composites may not favor Cr(VI) reduction owing to their inherent electronic structure. Basically, copper and vanadium exist in the +2 and +5 oxidation states, respectively, in Cu$_3$V$_2$O$_8$.[78] Vanadium in its +5 oxidation state is

**Fig. 8** (a) Photocatalytic reduction of 100 mg $L^{-1}$ Cr(VI) solution using pristine AV, RPOM, and RPOM−AV composites as catalysts (inset: colour change observed before and after light irradiation). (b) Rate constants for Cr(VI) reduction using pristine AV, RPOM, and RPOM−AV composites as catalysts. (c) UV-Visible absorption spectra of Cr(VI) with the help of the RPOM−AV2 composites. (d) Recyclability of the RPOM−AV2 composites after several successive cycles of Cr(VI) reduction in the presence of a 300 W Xenon lamp.

extremely stable and does not readily lose electrons. In addition, the +2 oxidation state of Cu is highly stable, and $Cu^{2+}$ is reluctant to donate its electrons and attain higher oxidation states. Therefore, copper vanadate-based composites are not conducive to electron donation and do not promote Cr(VI) reduction.

### 3.10.  Charge transfer mechanism

According to the positions of the energy bands of pristine metal vanadates and polyoxometalates determined from the Mott–Schottky analysis and bandgap calculation from the Tauc plots, it is observed that the charge transfer occurs through the indirect Z-scheme mechanism for both RPOM–AV and RPOM–CV nanocomposites with RGO acting as the solid-state electron-mediator. Conceptually, indirect Z-scheme heterojunctions are formed when the charge transfer occurs through an electron-mediator between one semiconductor with highly negative conduction band edge potential (reduction catalyst) and another semiconductor with highly positive valence band edge potential (oxidation catalyst).[79–81] The indirect Z-scheme
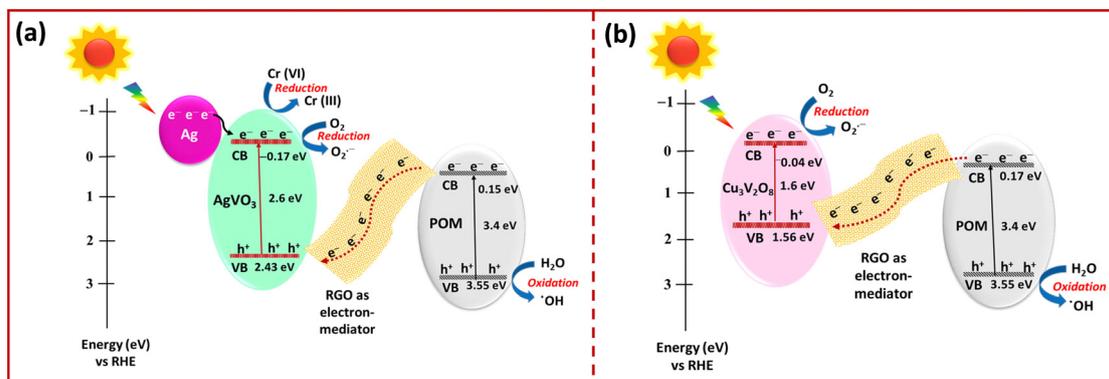


**Fig. 9** Charge transfer mechanism in (a) RPOM−AV and (b) RPOM−CV composites.

mechanism promotes the transfer of photogenerated charge carriers through the redox mediator and lowers electron–hole recombination.[82–86] The schematic presentation for the Cr(vi) reduction by RPOM–AV composites is displayed in Fig. 9a. In the presence of visible light, the generation of electron–hole pairs occurs in pristine AgVO$_3$ and POM. Moreover, electron–hole pairs are generated within the metallic silver nanoparticles in the presence of visible light owing to the surface plasmon resonance effect and dipolar character of metallic Ag. The plasmon-induced electrons of metallic Ag are transferred to the conduction band of AgVO$_3$. RGO present at the interface of the two pristine semiconductors acts as an electron-mediator and provides efficient charge transfer channels to promote the excellent transfer of photogenerated electrons present in the conduction band of POM to recombine with the holes present in the valence band of AV. Therefore, the electrons with greater reducing capability, which are fully retained in the conduction band of AV, perform the reduction of toxic Cr(vi).

A similar charge transfer mechanism also occurs for the RPOM–CV composites, as illustrated in Fig. 9b. In the presence of light, charge carriers are generated in bare CV and POM. RGO acts as an electron-mediator to promote electron transfer, and the electrons present in the conduction band of POM recombine with the holes in the valence band of pristine CV. Therefore, the electrons with strong reduction ability are preserved in the conduction band of CV. The holes with greater oxidizing power, which are reserved in the valence band of POM, perform the oxidation of the MB dye.

## 4. Conclusion

In summary, polyoxometalate-loaded RGO-based metal vanadates were synthesized *via* a facile co-precipitation method, and their photocatalytic activity was explored in visible light. It was observed that the RPOM–AV composites with an optimized loading of metal precursors exhibited photocatalytic Cr(vi) reduction of up to 94% within 60 minutes and 94% removal of the RB dye in 120 minutes through adsorption owing to its large surface area. The RPOM–CV composites showed 96% photocatalytic degradation of MB dye after 5 hours in the presence of visible light. Moreover, it is evident from the photoelectrochemical investigation that the RPOM–AV and RPOM–CV composites exhibit 51 times and 6 times enhancement in the photocurrent density in comparison with pristine AV and CV, respectively, as a result of the remarkable augmentation in the donor density upon the incorporation of RPOM into metal vanadates. Additionally, the quenching of the photoluminescence intensity reflects the lower rate of electron–hole recombination after composite formation. The superior photocatalytic activity of the RPOM-based metal vanadate composites can be attributed to the development of the indirect Z-scheme heterojunction with RGO acting as the solid-state electron mediator. Therefore, our results indicate that polyoxometalate-based metal vanadates provide a novel paradigm for the development of efficient visible-light active photocatalysts for environmental remediation.

## Data availability

The data supporting this article have been included as a part of the ESI.†

## Conflicts of interest

The authors declare that they have no known competing financial interests or personal relationships that could have appeared to influence the work reported in this paper.

## Acknowledgements

## References

1 A. T. Hoang, A. Pandey, W.-H. Chen, S. F. Ahmed, S. Nižetić, K. H. Ng, Z. Said, X. Q. Duong, Ü. Ağbulut, H. Hadiyanto and X. P. Nguyen, Hydrogen Production by Water Splitting with Support of Metal and Carbon-Based Photocatalysts, *ACS Sustainable Chem. Eng.*, 2023, **11**, 1221–1252.

2 W. Qi, Y. Fu, E. Liu, Z. Cheng, Y. Sun, S. Liu and M. Yang, Advancements and opportunities in piezo-(photo)catalytic synthesis of value-added chemicals, *EES Catal.*, 2024, **2**, 884–910.

3 P. Ganguly, M. Harb, Z. Cao, L. Cavallo, A. Breen, S. Dervin, D. D. Dionysiou and S. C. Pillai, 2D Nanomaterials for Photocatalytic Hydrogen Production, *ACS Energy Lett.*, 2019, **4**, 1687–1709.

4 S. Ghosh, N. A. Kouamé, L. Ramos, S. Remita, A. Dazzi, A. Deniset-Besseau, P. Beaunier, F. Goubard, P.-H. Aubert and H. Remita, Conducting Polymer Nanostructures for Photocatalysis under Visible Light, *Nat. Mater.*, 2015, **14**, 505–511.

5 P. Ganguly, S. Mathew, L. Clarizia, R. S. Kumar, A. Akande, S. Hinder, A. Breen and S. C. Pillai, Theoretical and Experimental Investigation of Visible Light Responsive AgBiS$_2$–TiO$_2$ Heterojunctions for Enhanced Photocatalytic Applications, *Appl. Catal., B*, 2019, **253**, 401–418.

6 W. Xu, S. Lai, S. Pillai, W. Chu, Y. Hu, X. Jiang, M. Fu, X. Wu, F. Li and H. Wang, Visible Light Photocatalytic Degradation of Tetracycline with Porous Ag/Graphite Carbon Nitride Plasmonic Composite: Degradation Pathways and Mechanism, *J. Colloid Interface Sci.*, 2020, **574**, 110–121.

7 S. Feizpoor, A. Habibi-Yangjeh, D. Seifzadeh and S. Ghosh, Combining Carbon Dots and Ag$_6$Si$_2$O$_7$ Nanoparticles with TiO$_2$: Visible-Light-Driven Photocatalysts with Efficient

Performance for Removal of Pollutants, *Sep. Purif. Technol.*, 2020, **248**, 116928–116939.

8 K. Wang, Z. Bielan, M. Endo-Kimura, M. Janczarek, D. Zhang, D. Kowalski, A. Zielińska-Jurek, A. Markowska-Szczupak, B. Ohtani and E. Kowalska, On the Mechanism of Photocatalytic Reactions on $Cu_xO@TiO_2$ Core–Shell Photocatalysts, *J. Mater. Chem. A*, 2021, **9**, 10135–10145.

9 P. Kar, S. Sardar, B. Liu, M. Sreemany, P. Lemmens, S. Ghosh and S. K. Pal, Facile Synthesis of Reduced Graphene Oxide–Gold Nanohybrid for Potential Use in Industrial Waste-Water Treatment, *Sci. Technol. Adv. Mater.*, 2016, **17**, 375–386.

10 M. Méndez-Medrano, E. Kowalska, A. Lehoux, A. Herissan, B. Ohtani, S. Rau, C. Colbeau-Justin, J. L. Rodríguez-López and H. Remita, Surface Modification of $TiO_2$ with Au Nanoclusters for Efficient Water Treatment and Hydrogen Generation under Visible Light, *J. Phys. Chem. C*, 2016, **120**, 25010–25022.

11 H. She, R. Hua, J. Zhao, Y. Xia, L. Wang, J. Huang and Q. Wang, Synergetic regulation of interfacial electronic structure of Cu, N co-doped carbon modified $TiO_2$ for efficient photocatalytic $CO_2$ reduction, *Chem. Eng. J.*, 2024, **496**, 153799.

12 A. L. Luna, D. Dragoe, K. Wang, P. Beaunier, E. Kowalska, B. Ohtani, D. Bahena Uribe, M. A. Valenzuela, H. Remita and C. Colbeau-Justin, Photocatalytic Hydrogen Evolution Using Ni–Pd/$TiO_2$: Correlation of Light Absorption, Charge-Carrier Dynamics, and Quantum Efficiency, *J. Phys. Chem. C*, 2017, **121**, 14302–14311.

13 S. Yao, J. He, F. Gao, H. Wang, J. Lin, Y. Bai, J. Fang, F. Zhu, F. Huang and M. Wang, Highly Selective Semiconductor Photocatalysis for $CO_2$ Reduction, *J. Mater. Chem. A*, 2023, **11**, 12539–12558.

14 X. Xu, H. Wang, K. Chen, Q. Mei, J. Li and Q. Wang, Novel ternary composite catalyst 2H/1T-$MoS_2$/$Co_3O_4$-Ru for photoelectrocatalytic nitrogen reduction, *Chem. Eng. J.*, 2024, **485**, 149922.

15 X. Yuan, D. Floresyona, P.-H. Aubert, T.-T. Bui, S. Remita, S. Ghosh, F. Brisset, F. Goubard and H. Remita, Photocatalytic Degradation of Organic Pollutant with Polypyrrole Nanostructures under UV and Visible Light, *Appl. Catal., B*, 2019, **242**, 284–292.

16 S. Samajdar, A. Golda, S. K. Lakhera and S. Ghosh, Recent Progress in Chromium Removal from Wastewater Using Covalent Organic Frameworks – A Review, *Chemosphere*, 2024, **350**, 141028.

17 Y. Cui, Z. Wang, J. Zheng, B. Li, Y. Yan and M. Meng, Fabrication of Silver Vanadate Quantum Dots/Reduced Graphene Oxide/Graphitic Carbon Nitride Z-Scheme Heterostructure Modified Polyvinylidene Fluoride Self-Cleaning Membrane for Enhancing Photocatalysis and Mechanism Insight, *J. Colloid Interface Sci.*, 2022, **614**, 677–689.

18 S. Joseph, S. Abraham, R. N. Priyanka, T. Abraham, A. Suresh and B. Mathew, In Situ S-Doped Ultrathin G-$C_3N_4$ Nanosheets Coupled with Mixed-Dimensional (3D/1D) Nanostructures of Silver Vanadates for Enhanced Photocatalytic Degradation of Organic Pollutants, *New J. Chem.*, 2019, **43**, 10618–10630.

19 M. K. Hossain, P. Sotelo, H. P. Sarker, M. T. Galante, A. Kormányos, C. Longo, R. T. Macaluso, M. N. Huda, C. Janáky and K. Rajeshwar, Rapid One-Pot Synthesis and Photoelectrochemical Properties of Copper Vanadates, *ACS Appl. Energy Mater.*, 2019, **2**, 2837–2847.

20 S. Pulipaka, N. Boni and P. Meduri, Copper Vanadate ($Cu_3V_2O_8$): (Mo, W) Doping Insights to Enhance Performance as an Anode for Photoelectrochemical Water Splitting, *ACS Appl. Energy Mater.*, 2020, **3**, 6060–6064.

21 S. Bera, S. Ghosh and R. N. Basu, Silver as Solid-State Electron Mediator in $MoS_2$/Ag–$AgVO_3$ Z-Scheme Heterostructures for Photocatalytic $H_2$ Generation, *J. Alloys Compd.*, 2020, **830**, 154527–154539.

22 J. Yu, J. Dong, X. Su, J. Yang, D. Zhang, J. Liu, P. Cai, Z. Li, D. Zhang and X. Pu, Preparation and Characterization of $AgVO_3$/$Ag_4V_2O_7$/BiOI Double S-Scheme Heterojunctions for the Photocatalytic Degradation of Methylene Orange and Tetracycline, *J. Alloys Compd.*, 2024, **987**, 174187–174198.

23 C.-M. Jiang, G. Segev, L. H. Hess, G. Liu, G. Zaborski, F. M. Toma, J. K. Cooper and I. D. Sharp, Composition-Dependent Functionality of Copper Vanadate Photoanodes, *ACS Appl. Mater. Interfaces*, 2018, **10**, 10627–10633.

24 J. Guo, J. Liang, X. Yuan, L. Jiang, G. Zeng, H. Yu and J. Zhang, Efficient Visible-Light Driven Photocatalyst, Silver (Meta)Vanadate: Synthesis, Morphology and Modification, *J. Chem. Eng.*, 2018, **352**, 782–802.

25 J. Yang, J. Hao, S. Xu, Q. Wang, J. Dai, A. Zhang and X. Pang, $InVO_4$/β-$AgVO_3$ Nanocomposite as a Direct Z-Scheme Photocatalyst toward Efficient and Selective Visible-Light-Driven $CO_2$ Reduction, *ACS Appl. Mater. Interfaces*, 2019, **11**, 32025–32037.

26 Y. Song, X. Zhao, X. Feng, L. Chen, T. Yuan and F. Zhang, Z-Scheme $Cu_2O$/Cu/$Cu_3V_2O_7(OH)_2$·$2H_2O$ Heterostructures for Efficient Visible-Light Photocatalytic $CO_2$ Reduction, *ACS Appl. Energy Mater.*, 2022, **5**, 10542–10552.

27 W.-Y. Geng, X.-X. Lu, H. Zhang, Y.-H. Luo, Z.-X. Wang, S.-F. Guo, Z.-Y. Zhou and D.-E. Zhang, Effective Design and Synthesis of Donor-Acceptor Covalent Triazine Polymers with Boosted Photocatalytic Performance for Cr(VI) Reduction, *Sep. Purif. Technol.*, 2022, **290**, 120829–120839.

28 S. Y. Djoko T., E. Njoyim T., A. D. Nguyen, J. Yang, H. Küçükkeçeci, E. M. Kutorglo, B. Radhakrishnan, K. Schwarzburg, S. Huseyinova, P. Das, M. Tasbihi, M. Schwarze, A. Thomas and R. Schomäcker, Polyoxometalate (POM) Boosting the Light-Harvesting Ability of Graphitic Carbon Nitride for Efficient Photocatalytic Hydrogen Production, *Catal. Sci. Technol.*, 2024, **14**, 2114–2129.

29 J. Lan, Y. Wang, B. Huang, Z. Xiao and P. Wu, Application of Polyoxometalates in Photocatalytic Degradation of Organic Pollutants, *Nanoscale Adv.*, 2021, **3**, 4646–4658.

30 A. Solé-Daura, Y. Benseghir, M.-H. Ha-Thi, M. Fontecave, P. Mialane, A. Dolbecq and C. Mellot-Draznieks, Origin of the Boosting Effect of Polyoxometalates in Photocatalysis: The Case of $CO_2$ Reduction by a Rh-Containing Metal–Organic Framework, *ACS Catal.*, 2022, **12**, 9244–9255.

31  X. Chen, H. Wu, X. Shi and L. Wu, Polyoxometalate-Based Frameworks for Photocatalysis and Photothermal Catalysis, *Nanoscale*, 2023, **15**, 9242–9255.

32  R. Morita, Y. Murakami, X.-F. Shen, D. Yang, M. Watanabe, J. T. Song, A. Takagaki and T. Ishihara, Enhanced Charge Mediator Properties of Photocatalysts with Reduced Graphene Nanoribbons for Photocatalytic Acceleration of Hydrogen Production in Aqueous Media, *J. Mater. Chem. C*, 2024, **12**, 1652–1660.

33  M. S. Sadek, G. E. Khedr, M. F. A. Messih and M. A. H. Ismail, Experimental and DFT Study of Photocatalytic Activity of Reduced Graphene Oxide/Copper Sulfide Composite for Removal of Organic Dyes from Water, *Sci. Rep.*, 2023, **13**, 15636–15650.

34  M. Yang, D. S. Kim, T. J. Lee, S. J. Lee, K. G. Lee and B. G. Choi, Polyoxometalate-Grafted Graphene Nanohybrid for Electrochemical Detection of Hydrogen Peroxide and Glucose, *J. Colloid Interface Sci.*, 2016, **468**, 51–56.

35  X. Gao, J. Wang, Q. Xue, Y.-Y. Ma and Y. Gao, AgBr/Polyoxometalate/Graphene Oxide Ternary Composites for Visible Light-Driven Photocatalytic Hydrogen Production, *ACS Appl. Nano Mater.*, 2021, **4**, 2126–2135.

36  X.-H. Li, W.-L. Chen, H.-Q. Tan, F.-R. Li, J.-P. Li, Y.-G. Li and E.-B. Wang, Reduced State of the Graphene Oxide@Polyoxometalate Nanocatalyst Achieving High-Efficiency Nitrogen Fixation under Light Driving Conditions, *ACS Appl. Mater. Interfaces*, 2019, **11**, 37927–37938.

37  L. Yu, Q. Liu, S. Ding, J. Yu, S. Peng, J. Zhang, C. Jiang and G. Yang, The Assembly of Polyoxometalate-Graphene Oxide Composites for Photocatalytic Removal of Organic Dye in Water, *Appl. Surf. Sci.*, 2022, **602**, 154095–154105.

38  S. Saha, L. N. Zakharov, B. Captain and D. A. Keszler, Synthesis and Structural Analysis of Novel Phosphonium Hexatungstate Complexes, *J. Cluster Sci.*, 2021, **32**, 693–702.

39  H. Yu, B. Zhang, C. Bulin, R. Li and R. Xing, High-Efficient Synthesis of Graphene Oxide Based on Improved Hummers Method, *Sci. Rep.*, 2016, **6**, 36143–36150.

40  S. Ghosh, S. Bera, S. Sardar, S. Pal, F. V. A. Camargo, C. D'Andrea and G. Cerullo, Role of Efficient Charge Transfer at the Interface between Mixed-Phase Copper-Cuprous Oxide and Conducting Polymer Nanostructures for Photocatalytic Water Splitting, *ACS Appl. Mater. Interfaces*, 2023, **15**, 18867–18877.

41  S. Samajdar, S. Bera, P. S. Das, H. Finch, V. R. Dhanak, S. Chakraborty, T. Maiyalagan, K. Annapurna and S. Ghosh, Exploration of 1D-2D LaFeO$_3$/RGO S-Scheme Heterojunction for Photocatalytic Water Splitting, *Int. J. Hydrogen Energy*, 2023, **48**, 17838–17851.

42  S. Ghosh, H. Remita and R. N. Basu, Visible-Light-Induced Reduction of Cr(VI) by PDPB-ZnO Nanohybrids and Its Photo-Electrochemical Response, *Appl. Catal., B*, 2018, **239**, 362–372.

43  H.-H. Huang, K. K. H. De Silva, G. R. A. Kumara and M. Yoshimura, Structural Evolution of Hydrothermally Derived Reduced Graphene Oxide, *Sci. Rep.*, 2018, **8**, 6849–6858.

44  A. R. Thiruppathi, J. van der Zalm, C.-K. Hung and A. Chen, Synthesis and Electrochemical Studies of 3D Reduced Graphene Oxide for Efficient Energy Storage, *ACS Appl. Energy Mater.*, 2023, **6**, 5486–5497.

45  M. Pudukudy, Q. Jia, H. Wang, S. Shan and R. Rajendran, Influence of Synthesis Parameters on the Crystalline, Structural, Textural, Optical and Photocatalytic Properties of α and β Polymorphs of AgVO$_3$ Nanorods, *Mater. Sci. Semicond. Process.*, 2020, **107**, 104824–104835.

46  S. Choudhary, G. Kumawat, M. Khandelwal, R. K. Khangarot, V. Saharan, S. Nigam and Harish, Phyco-Synthesis of Silver Nanoparticles by Environmentally Safe Approach and Their Applications, *Sci. Rep.*, 2024, **14**, 9568–9581.

47  U. Holzwarth and N. Gibson, The Scherrer equation versus the 'Debye-Scherrer equation', *Nat. Nanotechnol.*, 2011, **6**, 534.

48  J. A. Seabold and N. R. Neale, All First Row Transition Metal Oxide Photoanode for Water Splitting Based on Cu$_3$V$_2$O$_8$, *Chem. Mater.*, 2015, **27**, 1005–1013.

49  W. Liu and G. Speranza, Tuning the Oxygen Content of Reduced Graphene Oxide and Effects on Its Properties, *ACS Omega*, 2021, **6**, 6195–6205.

50  K. K. H. De Silva, P. Viswanath, V. K. Rao, S. Suzuki and M. Yoshimura, New Insight into the Characterization of Graphene Oxide and Reduced Graphene Oxide Monolayer Flakes on Si-Based Substrates by Optical Microscopy and Raman Spectroscopy, *J. Phys. Chem. C*, 2021, **125**, 7791–7798.

51  A. A. K. King, B. R. Davies, N. Noorbehesht, P. Newman, T. L. Church, A. T. Harris, J. M. Razal and A. I. Minett, A New Raman Metric for the Characterisation of Graphene oxide and its Derivatives, *Sci. Rep.*, 2016, **6**, 19491–19497.

52  X. Kong, Z. Guo, C. Zeng, J. Huang, L. Cao, L. Li, L. Yin, P. Wen, Q. Feng and Z. Xu, Soft Chemical In Situ Synthesis, Formation Mechanism and Electrochemical Performances of 1D Bead-like AgVO3 Nanoarchitectures, *J. Mater. Chem. A*, 2015, **3**, 18127–18135.

53  A. Song, S. P. Berglund, A. Chemseddine, D. Friedrich, F. F. Abdi and R. van de Krol, Elucidating the Optical, Electronic, and Photoelectrochemical Properties of p-Type Copper Vanadate (p-Cu5V2O10) Photocathodes, *J. Mater. Chem. A*, 2020, **8**, 12538–12547.

54  S. Ghosh, Y. Holade, H. Remita, K. Servat, P. Beaunier, A. Hagège and T. W. Napporn, One-pot synthesis of reduced graphene oxide supported gold-based nanomaterials as robust nanocatalysts for glucose electrooxidation, *Electrochim. Acta*, 2016, **212**, 864–875.

55  G. Murmu, S. Samajdar, S. Ghosh, K. Shakeela and S. Saha, Tungsten-Based Lindqvist and Keggin Type Polyoxometalates as Efficient Photocatalysts for Degradation of Toxic Chemical Dyes, *Chemosphere*, 2023, **346**, 140576–140588.

56  J. S. Jayan, B. D. S. Deeraj, K. Joseph and A. Saritha, Designed and Tailor-Made Double Hydrophilic Block Copolymer-Graphene Nanoplatelet Hybrids for Reinforcing Epoxy Thermosets, *Sci. Rep.*, 2024, **14**, 8812–8828.

57 K. K. Mandari, N. Son, T. Kim and M. Kang, Highly Efficient $SnS_2$@Ag/$AgVO_3$ Heterostructures for Improved Charge Carriers in Photocatalytic $H_2$ Production, *J. Alloys Compd.*, 2022, **927**, 166886–166897.

58 Q. Liu, N. Chen, S. Bai and W. Li, Effect of Silver Nitrate on the Thermal Processability of Poly(Vinyl Alcohol) Modified by Water, *RSC Adv.*, 2018, **8**, 2804–2810.

59 B. D. Ossonon and D. Bélanger, Synthesis and Characterization of Sulfophenyl-Functionalized Reduced Graphene Oxide Sheets, *RSC Adv.*, 2017, **7**, 27224–27234.

60 Y. Liang, P. Liu, H. B. Li and G. W. Yang, Synthesis and Characterization of Copper Vanadate Nanostructures via Electrochemistry Assisted Laser Ablation in Liquid and the Optical Multi-Absorptions Performance, *CrystEngComm*, 2012, **14**, 3291–3296.

61 I. Khan and A. Qurashi, Shape Controlled Synthesis of Copper Vanadate Platelet Nanostructures, Their Optical Band Edges, and Solar-Driven Water Splitting Properties, *Sci. Rep.*, 2017, **7**, 14370–14381.

62 R. Sadek, M. S. Sharawi, C. Dubois, H. Tantawy and J. Chaouki, Superior Quality Chemically Reduced Graphene Oxide for High Performance EMI Shielding Materials, *RSC Adv.*, 2022, **12**, 22608–22622.

63 J. Chellappa, S. D. Abraham, R. B. Bennie and A. Naveen, Microwave Assisted Synthesis, Characterization and Photocatalytic Activity of $Zn_2V_2O_7$ Nanospheres, *Chem. Sci. Trans.*, 2014, **3**, 1488–1496.

64 A. Kuila, N. Maity, R. K. Layek and A. K. Nandi, On the pH sensitive optoelectronic properties of amphiphilic reduced graphene oxide via grafting of poly(dimethylaminoethyl methacrylate): a signature of p- and n-type doping, *J. Mater. Chem. A*, 2014, **2**, 16039–16050.

65 P. Sinha, A. Datar, C. Jeong, X. Deng, Y. G. Chung and L.-C. Lin, Surface Area Determination of Porous Materials Using the Brunauer–Emmett–Teller (BET) Method: Limitations and Improvements, *J. Phys. Chem. C*, 2019, **123**, 20195–20209.

66 D. Kundu, G. Murmu, S. Zamindar, N. C. Murmu, P. Banerjee and S. Saha, Tetraalkyl/Alkyltriphenyl phosphonium Hexatungstates for Efficient Electrocatalytic Hydrogen Evolution Reaction in Alkaline Media: An Experimental and In Silico-Based Synchronization Approach, *ACS Appl. Energy Mater.*, 2024, **7**, 8423–8435.

67 K. Sivula, Mott−Schottky Analysis of Photoelectrodes: Sanity Checks Are Needed, *ACS Energy Lett.*, 2021, **6**, 2549–2551.

68 S. Ghosh, P. S. Das, D. Sarkar, S. Pal, M. K. Naskar, Y. S. Chaudhary, S. Dey and C. Sinha, Z-Scheme Heterostructures Using Band-Gap-Tunable ZnO by Metal Doping and Coupling with Polypyrrole for Enhanced Photocatalytic Water Splitting, *ACS Appl. Polym. Mater.*, 2023, **5**, 9918–9930.

69 M. A. Rauf and S. S. Ashraf, Fundamental Principles and Application of Heterogeneous Photocatalytic Degradation of Dyes in Solution, *Chem. Eng. J.*, 2009, **151**, 10–18.

70 D. Heger, J. Jirkovský and P. Klán, Aggregation of Methylene Blue in Frozen Aqueous Solutions Studied by Absorption Spectroscopy, *J. Phys. Chem. A*, 2005, **109**, 6702–6709.

71 S. Kim, J. Yeo and W. Choi, Simultaneous conversion of dye and hexavalent chromium in visible light-illuminated aqueous solution of polyoxometalate as an electron transfer catalyst, *Appl. Catal., B*, 2008, **84**, 148–155.

72 F. Chen, Q. Yang, Y. Wang, F. Yao, Y. Ma, X. Huang, X. Li, D. Wang, G. Zeng and H. Yu, Efficient Construction of Bismuth Vanadate-Based Z-Scheme Photocatalyst for Simultaneous Cr(VI) Reduction and Ciprofloxacin Oxidation under Visible Light: Kinetics, Degradation Pathways and Mechanism, *J. Chem. Eng.*, 2018, **348**, 157–170.

73 R. Yang, Z. Zhu, C. Hu, S. Zhong, L. Zhang, B. Liu and W. Wang, One-Step Preparation (3D/2D/2D) $BiVO_4$/$FeVO_4$@rGO Heterojunction Composite Photocatalyst for the Removal of Tetracycline and Hexavalent Chromium Ions in Water, *Chem. Eng. J.*, 2020, **390**, 124522–124537.

74 P. Liu, J. Yi, R. Bao and H. Zhao, Theory-Oriented Synthesis of 2D/2D $BiVO_4$/MXene Heterojunction for Simultaneous Removal of Hexavalent Chromium and Methylene Blue, *ChemCatChem*, 2021, **13**, 3046–3053.

75 S. Asoubar, A. Mehrizad, M. A. Behnajady, M. E. Ramazani and P. Gharbani, Hexavalent Chromium Reduction and Rhodamine B Degradation by Visible-Light-Driven Photocatalyst of Stannum Indium Sulfide-Samarium Vanadate, *npj Clean Water*, 2023, **6**, 27–38.

76 P. Babu, S. Mohanty, B. Naik and K. Parida, Serendipitous Assembly of Mixed Phase $BiVO_4$ on B-Doped g-$C_3N_4$: An Appropriate p–n Heterojunction for Photocatalytic $O_2$ Evolution and Cr(VI) Reduction, *Inorg. Chem.*, 2019, **58**, 12480–12491.

77 J. Jia, M. Zhang, Z. Liu, C. Yu, W. Zhou and Z. Li, $La^{3+}$, $Gd^{3+}$-Codoped $BiVO_4$ Nanorods with Superior Visible-Light-Driven Photocatalytic Performance for Simultaneous Removing Aqueous Cr(VI) and Azo Dye, *J. Nanoparticle Res.*, 2020, **22**, 275–289.

78 C.-M. Jiang, M. Farmand, C. H. Wu, Y.-S. Liu, J. Guo, W. S. Drisdell, J. K. Cooper and I. D. Sharp, Electronic Structure, Optoelectronic Properties, and Photoelectrochemical Characteristics of $\gamma$-$Cu_3V_2O_8$ Thin Films, *Chem. Mater.*, 2017, **29**, 3334–3345.

79 J. Zhou, J. Li, L. Kan, L. Zhang, Q. Huang, Y. Yan, Y. Chen, J. Liu, S.-L. Li and Y.-Q. Lan, Linking Oxidative and Reductive Clusters to Prepare Crystalline Porous Catalysts for Photocatalytic $CO_2$ Reduction with $H_2O$, *Nat. Commun.*, 2022, **13**, 4681–4691.

80 J.-C. Wang, H.-C. Yao, Z.-Y. Fan, L. Zhang, J.-S. Wang, S.-Q. Zang and Z.-J. Li, Indirect Z-Scheme BiOI/g-$C_3N_4$ Photocatalysts with Enhanced Photoreduction $CO_2$ Activity under Visible Light Irradiation, *ACS Appl. Mater. Interfaces*, 2016, **8**, 3765–3775.

81 V. D. Dang, J. Adorna, T. Annadurai, T. A. N. Bui, H. L. Tran, L.-Y. Lin and R.-A. Doong, Indirect Z-Scheme Nitrogen-Doped Carbon Dot Decorated $Bi_2MoO_6$/g-$C_3N_4$ Photocatalyst for Enhanced Visible-Light-Driven Degradation of Ciprofloxacin, *J. Chem. Eng.*, 2021, **422**, 130103.

82 Y. Baghdadi, M. Daboczi, F. Temerov, M. Yang, J. Cui and S. A. Eslava, A G-$C_3N_4$/RGO/$Cs_3Bi_2Br_9$ Mediated Z-Scheme Heterojunction for Enhanced Photocatalytic $CO_2$ Reduction, *J. Mater. Chem. A*, 2024, **12**, 16383–16395.

83 F. Wu, X. Li, W. Liu and S. Zhang, Highly Enhanced Photocatalytic Degradation of Methylene Blue over the Indirect All-Solid-State Z-Scheme g-C$_3$N$_4$-RGO-TiO$_2$ Nanoheterojunctions, *Appl. Surf. Sci.*, 2017, **405**, 60–70.

84 S. Nayak and K. M. Parida, Deciphering Z-Scheme Charge Transfer Dynamics in Heterostructure NiFe-LDH/N-RGO/g-C$_3$N$_4$ Nanocomposite for Photocatalytic Pollutant Removal and Water Splitting Reactions, *Sci. Rep.*, 2019, **9**, 2458–2481.

85 A. Iwase, Y. H. Ng, Y. Ishiguro, A. Kudo and R. Amal, Reduced Graphene Oxide as a Solid-State Electron Mediator in Z-Scheme Photocatalytic Water Splitting under Visible Light, *J. Am. Chem. Soc.*, 2011, **133**, 11054–11057.

86 L. Wang, G. Huang, L. Zhang, R. Lian, J. Huang, H. She, C. Liu and Q. Wang, Construction of TiO$_2$-covalent organic framework Z-Scheme hybrid through coordination bond for photocatalytic CO$_2$ conversion, *J. Energy Chem.*, 2022, **64**, 85–92.